Complex and confined laboratory ruptures explain scaling of the critical slip distance for earthquake faulting

Srisharan Shreedharan[1*], Luc Lavier[2,3] and Chris Marone[4,5]

[1]Department of Geosciences, Utah State University, UT, USA

[2]Institute for Geophysics, Jackson School of Geosciences, University of Texas at Austin, TX, USA

[3]Department of Geological Sciences, Jackson School of Geosciences, University of Texas at Austin, TX, USA

[4]Department of Geosciences, The Pennsylvania State University, PA, USA

[5]Dipartimento di Scienze della Terra, La Sapienza Università di Roma, Italy

*Corresponding author.

Email: srisharan.shreedharan@usu.edu

This PDF file includes:

Main Text
Methods
References
Figures 1 to 4

Abstract

Earthquake sequences in nature are complex, exhibiting a range of magnitudes and slip behaviors. In contrast, earthquake-like instabilities generated on frictional faults in the laboratory and in continuum numerical models are usually quasi-periodic with a smaller range of magnitudes and durations. The discrepancy, especially apparent for cm-sized samples used in lab friction experiments, has been attributed to complex multi-fault interactions in nature and heterogeneities in stress state or strength of seismogenic faults. Here, we provide another explanation by combining laboratory experiments and numerical models of fully deformable faults that show complex rupture sequences and fully confined slip events. We observe complex rupture sequences even on simple, initially homogeneous faults ranging from a few centimeters, in the lab, to tens of kilometers in numerical models. Our results show that self-generated heterogeneities on lab faults can produce slow and complex ruptures that may be fully confined on mm-scale faults, challenging the long-held idea that such lab faults fail only as rigid blocks. We also document complex behaviors including aperiodicity and significant variability in rupture properties over short timescales due to local, self-generated heterogeneities in stress and friction strength. Our simulations show that the ratio of fault zone thickness to the critical slip distance, Dc, controls the observed failure mode, with wider shear zones and larger Dc giving rise to slower slip events. We demonstrate (a) that complex rupture behaviors can arise even on initially homogeneous faults, and (b) that the same fault may accommodate a spectrum of earthquake slip modes at different scales.

Introduction

Earthquakes are frictional instabilities usually described by constitutive relationships linking the evolution of fault frictional strength with fault slip rate and slip history (*1,2*). In nature, earthquake sequences are often complex and exhibit a range of slip speeds, durations, and magnitudes, all within a given geologic setting and over comparable timescales (*3*). This complexity is usually attributed to multi-fault interactions during earthquake sequences (*4,5*) and the highly heterogeneous nature of crustal faults with spatially varying distributions in stress, fluids, lithology, and fault geometry (*6,7,8*). This interpretation is further bolstered by observations of quasi-periodic frictional instabilities or 'stick-slips' in the laboratory (*9,10*) and continuum numerical models of earthquake cycles (*11,12,13,14*) which exhibit a narrow range of event sizes and recurrence intervals in uniformly homogeneous faults over a range of initial and boundary conditions. However, a limited number of multi-cycle earthquake simulations (*15,16,17,18*) and large, meter-scale friction experiments (*19*) have documented that homogeneous faults can also exhibit complex rupture behaviors without the presence of external heterogeneities when the fault dimension is sufficiently larger than some characteristic length-scale determined by constitutive laws governing frictional slip or due to spontaneously developing stress heterogeneities.

Here, we demonstrate that initially homogeneous elastic faults can exhibit complex rupture behaviors such as confined ruptures for a wide range of spatial scales without externally imposed heterogeneities. Our lab results are explained by numerical results showing that complex rupture behaviors can arise even on initially homogeneous faults through spatially coherent stress heterogeneities that develop naturally during repetitive seismic cycles.

We utilize our numerical model to introduce a framework for scaling the critical slip distance (Dc, a characteristic length scale of frictional slip) with fault zone thickness and the degree of shear localization, as has been observed in the lab (*20*). Geologic studies of fault zones also document the role of shear localization, and our models provides a direct link between localization, fault zone compliance, and strain rate. By incorporating an explicit dependence of Dc on fault zone

thickness, our numerical models reproduce the full spectrum of tectonic slip modes, from stable creep and slow slip events to fast earthquakes, at different scales on the same homogeneous fault.

The critical slip distance (Dc) in the context of rate-state friction represents the slip required to reset the frictional memory of sheared microscopic contact junctions (or asperities) (*20,21,22,23*). Friction experiments on rough and planar faults including cases with wear material (known as fault gouge) 1-10 mm wide where strain localizes over 10-100s of microns (*20*) yield Dc values of 1 to a few hundred micrometers (*2,24,25*). For shear within finite-width fault zones (or fault gouges), which are more realistic representations of mature earthquake faults than planar cracks, Dc may be a proxy for the thickness of the zone, H, where shear strain is localized (*16,20,25,26*). This interpretation is further supported by field studies showing that slow slip tends to occur in complex, wide shear zones (*27,28,29*).

However, the implication of a likely relationship between Dc and fault zone thickness for the range of tectonic slip modes, from aseismic creep and slow slip to dynamic ruptures, is unclear, especially as numerical models of earthquake rupture generally approximate fault zones as elastic cracks of zero thickness (*13,17*). Direct observations of the thickness of fault zones indicates a range of process zone widths and the possibility that structures of different sizes may host different slip styles within the same fault zone (*27,28,29*). This introduces the possibility that the same fault could have different effective critical length scales depending upon the scale of deformation and strain localization. A major stumbling block for progress in understanding earthquake nucleation and the spectrum of fault slip behaviors is that detailed lab experiments to measure friction constitutive properties on samples larger than a few cm in size are rare. Moreover, numerical models for elastodynamic rupture are usually unable to resolve fault patch dimensions less than one meter, which is much larger than those indicated by lab experiments using the gouge particle sizes found in nature. Here, we circumvent this issue through a numerical model that simultaneously incorporates variations in Dc with fault zone thickness while accounting for possible spatiotemporal variations in fault slip. We integrate observations of lab faults with numerical models of km-scale faults and structural observations of shear zones to illuminate the importance of Dc for tectonic faulting, as a constitutive property rather than merely as a convenient fitting parameter. We focus here on Dc within the framework of rate-and-state friction (RSF). However, similar definitions of breakdown distance exist for other friction constitutive relationships, such as for the linear slip weakening law (*30*), and thus the framework we propose may be more widely applicable.

Results

Complex ruptures in homogeneous experimental and numerical faults

We generate a finite-width fault zone model (see Methods-Numerical model) that is intended to mimic laboratory friction experiment to demonstrate that complex frictional instabilities arise spontaneously on simple and homogeneous mm-scale faults. The lab earthquakes (stick-slip events) occur on faults of area 5 cm x 5 cm containing quartz gouge (see Methods-Friction experiments) which is externally loaded via an elastic spring. Both the laboratory friction experiment, henceforth referred to as the single direct-shear (SDS) experiment, and the numerical model include a single fault/shear zone of finite thickness (3 mm) being sheared at a prescribed loading rate (and strain rate) at a constant effective normal stress (Fig. 1a, b). While small-scale laboratory experiments are often described as a single-degree-of-freedom (SDOF) rigid spring-block slider (*31*), our results challenge this view. Our numerical model is composed of a deformable mesh of elastically interacting SDOF nodes which represents fault patches that interact with an external spring and with each other elastically and via radiation damping (Fig. 1b) (*12*).

Our lab and numerical results show small-scale rupture dynamics that are typically unmeasured in standard laboratory rock friction experiments, except in rare cases (e.g. *32*). Our SDS lab experiment was performed at 21 MPa effective normal stress, which is close to the critical stability boundary separating stable from unstable frictional sliding ($0.95 < \kappa < 1$; where κ is the

ratio of fault stiffness k to critical stiffness K_c) (*9,33,34*). Far below the stability boundary, lab earthquakes are quasi-periodic (nearly constant and highly predictable recurrence interval) or sometimes bimodal (alternating between two recurrence intervals, also referred to as period-doubling) (*9,34*). Very close to the stability boundary, complex and apparently aperiodic frictional behavior has been documented (Fig. 1c) (*9,10,34,35*) although its origins are poorly understood. Part of the complex pattern of small and large lab earthquakes seen in Fig. 1c has been attributed to deterministic chaos or complex behaviors associated with two (or more) interacting state variables or slider blocks describing the fault surface (*15*,*16,36,37,38,39*). In this context, deterministic chaos refers to frictional behavior that is apparently aperiodic, i.e, irregular in time, but highly sensitive to initial loading conditions. Here, we focus on the long period modulation of labquake stress drops (Fig. 1c). These events show systematic changes in stress drop that grow and then decrease over several cycles in a repeated manner (Fig. 1c). Whereas the variations in stress drop with slip rate are predicted by RSF laws, this long period modulation of labquake stress drop is not understood. We verified that these are not a byproduct of our shear configuration by reproducing them in both SDS and double direct shear loading configurations. They have also been documented in previous experiments (*9*,*10,24,40*). Here, we utilize this highly non-linear parameter-space of the SDS experiments to compare to the numerical model since it represents a strong test of the model's ability to well-reproduce the dynamics of lab faults, and by proxy, the internal interactions within the deformable fault model. The frictional and elastic properties used in the numerical model, along with the source of the values used are given in Supplementary Table S1.

For two different loading rates (4 μm/s and 13 μm/s), the numerical model matches the lab data and reproduces similar variations in the average stress drop over time (Fig. 1c, d). Moreover, the absolute values of stress drops averaged over the 5 cm long fault, slip durations, recurrence intervals and co-seismic slip amounts are equivalent for the SDS experiment and model (Supplementary Fig. S1a,b). The model predicts the same relationship between slip and labquake duration (Supplementary Fig. S1a) as the lab data. The slight differences in fault slip and stress drop may be because fault slip in our SDS experiments is not measured directly but estimated from an assumption of rigid block spring-slider (Equation 1) which overpredicts slip. In the SDS experiments, we measure the fault-averaged shear stress directly at the load-point, i.e., top of the central forcing steel block using a load cell, whereas in the numerical models, the stress drop is averaged across all nodes that experience slip during a rupture (See Methods). Minor differences between the lab and numerical results notwithstanding, the model well-reproduces the overall dynamics of the lab experiment. This demonstrates that the elastic and frictional parameters estimated from our lab experiments and used in the numerical model, are appropriate to describe the mechanics of experimental frictional instabilities.

The numerical model reveals the existence of a complex spatiotemporal evolution of slip events (Fig. 2a and Supplementary Fig. S2). These data show numerous confined ruptures that migrate along the fault at 0.1 – 1 mm/s. Although the fault experiences elevated slip rates during these instabilities, the peak slip rates are only 1-3 orders of magnitude higher than the loading rates (4 or 13 μm/s), indicating that these ruptures are self-propagating, quasi-dynamic events. They are relatively slow even though the fault experiences local slip rates of up to 1 mm/s. The frictional and elastic properties of the model, derived from friction experiments on quartz gouge (Supplementary Table S1, G = 200 MPa, σ_{eff}= 21 Mpa, b-a = 0.0031, Dc = 1.8 μm), can be used to estimate the critical nucleation patch size (L_c) for these ruptures, which represents the size of a quasistatic slip patch that is just large enough to initiate dynamic runaway and unstable sliding (*17,33,41*). The theoretical estimate of L_c for our model is ~5.5 mm and this matches the length/spatial extent of the confined ruptures (Fig. 2a and Supplementary Fig. S2). This indicates that such ruptures, occurring near the frictional stability boundary, do not span the entire fault even in the small, relatively rigid samples used in our lab experiments, which have a well-developed shear zone. This

is surprising and challenges the long-held assertion that small (< 10 cm) experimental faults slip as rigid blocks (*9,31*). Although we do not directly observe rupture propagation in the laboratory experiment due to the scope of experimental design (visualizing rupture propagation will require transparent layers or ultrasonic tomography), a recent study (*42*) has confirmed that such confined ruptures on 5 – 10 cm long faults may be observable in clay gouges over a limited range of boundary conditions.

Observations of the evolution of slip rate and shear stress at different locations along the fault in the numerical model (Fig. 2b) further clarify the complex nature of these ruptures. At a given location along the fault, the events are highly aperiodic and variable in size (stress drop, peak slip velocity, slip duration) with a combination of short periods of aseismic creep, creep transients, slow slip and fast ruptures all within a short timespan (< 100 s in Fig. 2b). Our lab and numerical observations suggest that these behaviors arise from self-generated heterogeneity and short-range elastic interactions between migrating ruptures modulated by residual prestress from previous ruptures. We cannot directly measure such transients and confined slip events in our 50 mm lab fault due to a lack of along-fault instrumentation. However, the numerical model provides an explanation for the occurrence of complex friction behaviors and the likely existence of migrating, confined ruptures along the mm-scale lab faults when the fault stiffness is comparable to the critical stiffness. This mechanism requires neither the use of additional state variables (*37*), nor explicit heterogeneities (*16,17*) in the fault to produce complex aperiodicity; instead, the stress heterogeneities are intrinsically produced (Supplementary Fig. S3) as a result of the initial conditions and evolution of fault properties, i.e., via frictional memory of strain history.

Discussion

The destabilizing effect of increasing normal stress

Existing lab studies (*9,10,19,34*) and our results demonstrate that the full range of slip modes from slow and complex to fast can be produced on a single fault, with no change in friction constitutive properties, by varying the normal stress. At lower normal stresses where the effective fault weakening rate is close to the critical frictional stiffness K_c, the model produces stable creep and quasi-periodic vibrations (Fig. 3a, 3b). As the normal stress is increased, we document an increase in aperiodic and complex slip behavior with a range of stress drops, slip speeds, durations, and varying degrees of partially confined ruptures (Fig. 3a, 3c), indicating that some degree of frictional memory in the strain history manifests as implicit stress heterogeneities in an otherwise homogeneous fault. Finally, at sufficiently large normal stress, we document periodic, rigid block-like behavior, as is typically expected for small mm-scale faults (Fig. 3a, 3d) (*9*).

This can be directly observed by documenting the stress state along the fault before and after multiple ruptures for the 21 MPa and 32 MPa simulations (Supplementary Figs. S3, S4). At lower stresses where confined ruptures and chaotic frictional behaviors are documented, the stress heterogeneities are small relative to the background shear strength and pervasive across the fault. This creates numerous rupture nucleation sites and adjacent barriers (Supplementary Fig. S3). Conversely, the high normal stress simulations are marked by a relatively uniform stress state across the fault prior to rupture, except at/near the rupture nucleation site which has a large stress heterogeneity (Supplementary Fig. S4). The uniformly high stress state along the propagation front allows the rupture to propagate over the entire fault.

The destabilizing behavior of normal stress in our mm-scale numerical models is consistent with experimental observations of stick-slip instabilities in fault gouge which exhibit an increase in fast ruptures at higher normal stresses (*9,24*). This is because the fault is far from the critical stability boundary at higher normal stresses (*9,33*). However, the degree of complexity is significantly greater near the transition from stable creep to unstable frictional motion (Figs. 1-3).

Scaling of Dc with fault zone width and loading rate

Using the numerical model of the mm-scale lab experiments, we conduct a series of earthquake rupture simulations (Fig. 4a) to explore multi-scale fault slip complexity. We use the same fault frictional and elastic properties (Supplementary Table S2) and explore fault thicknesses that range over five orders of magnitude (1.5 km to 15 cm). By fault thickness, here we refer to the width of the zone over which accumulated shear strain may be distributed (*15*,*43*), and make the assumption that strain is distributed uniformly over this thickness. Starting with the largest fault, we also vary Dc from 2 μm (for the 15 cm thick fault) to 20 mm (for the 1.5 km thick fault) and correspondingly the fault thickness (from 15 cm to 1.5 km) which, in turn, along with the far-field (plate) velocity modulates the strain rate at which the fault is loaded. Changing the fault zone thickness, and indirectly, compliance and strain rate, with Dc allows us to test the hypothesis that faults of different scales/sizes may have different critical frictional weakening distances associated with them. Across the suite of simulations, we ensure that the ratio of fault thickness (H) and Dc (or L_c), and all frictional/mechanical parameters remain constant. In other words, each numerical model represents a fully homogeneous fault with a different thickness such that H/Dc is constant. The values of Dc used allow the faults to remain close to the critical stability boundary ($\kappa \sim 1$) so that we document slow earthquakes at all scales although the rupture source properties may vary. Here, we define slow earthquakes as those with maximum slip rates not exceeding 100 times the value of the far field plate motion, consistent with the distinction made in previous numerical and lab studies (*9, 44*). Further, varying fault length with Dc ensures computational efficiency, since the timestep sizes depend on Dc (see Methods – Numerical model).

We drive the largest fault simulation at a representative convergent margin plate rate of 10^{-9} m/s and drive each subsequently smaller simulation at a far-field rate approximately equivalent to the peak slip rates for the next largest fault, i.e., an order of magnitude higher than the far-field rate. The rationale here is that progressively smaller faults or narrower shear zones embedded in larger fault zones may experience elevated strain rates (a) intrinsically by virtue of being thinner and (b) by concurrently being driven at higher-than-plate-rate during a slow transient or SSE (*29*). This means that across the simulations, the fault experiences strain rates from 10^{-14} – 10^{-6} s^{-1}, i.e., a two-order of magnitude jump in strain rates between successively smaller fault models.

The slow and fast ruptures simulated in our numerical models have seismic moments (M) in the range of 0.1 – 10^{16} Nm (M_w from -6 to 5) and characteristic slip durations (T) ranging from 10^{-2} – 10^{9} s (Fig. 4a). This corresponds to events in nature that can be detected geodetically such as slow slip events (SSEs) and seismically (e.g., Low frequency earthquakes – LFEs, very low frequency earthquakes – VLFEs etc.) (*45*). It also represents events that are difficult to identify due to detection limits of existing sensors. In the absence of surface signatures of crustal deformation or seismic radiation in our models, we calculate slip duration and moment differently than for natural earthquakes (see Methods – Estimation of rupture properties in the numerical model). Each of our model scenarios produces several ruptures (>100) and overall, the rupture duration is directly related to the seismic moment in a logarithmic sense (Fig. 4a). For the same elastic and frictional properties, slowly driven faults with wider shear zones, and therefore larger values of Dc, produce SSEs. Conversely, narrower faults with smaller Dc experience elevated strain rates and produce faster and smaller events with slip durations that resemble VLFEs and LFEs (Fig. 4a). The largest events produced in our models are SSEs that last for ~30 years, consistent with long-duration SSEs that may silently accommodate shallow slip deficit globally (*46,47*). The ruptures simulated in this study have significantly smaller moments than observed for natural ruptures. This is because (a) of the smaller fault lengths we have adopted (for computational efficiency) and (b) our model fault has no along-strike resolution. Thus, the seismic moments are significantly underestimated compared to natural slow-motion ruptures which have larger spatial dimensions (*48*).

Apparent differences in the moment-duration scaling for slow vs. fast earthquakes has been a longstanding discussion (*49*). One idea is that slow earthquakes represent different physical processes and scaling between M and T for slow ruptures is linear ($M \propto T$) whereas it is cubic for

elastodynamic ruptures ($M \propto T^3$). Existing lab work shows that the same physics and frictional processes can explain the full spectrum of slip modes. Our results also indicate that slow and fast slip modes occur via the same mechanisms and do not require different rupture mechanics. This is consistent with recent observations of SSE properties in Mexico (*50*), Cascadia (*51*) and San Andreas (*52*), which indicate that SSEs and other slow earthquake modes also follow a cubic moment-duration relationship. Numerical models of SSEs with size-dependent rupture velocities and stress drops also reproduce the cubic scaling relationships (*18*).

In our numerical study, there exists an approximately cubic relationship between M and T as $M \propto T^3$ within each model (Supplementary Fig. S5), whereas the overall trend across the suite of models more closely follows the relationship of $M \propto T$. The cubic relationship within a model arises as a direct consequence of the linear relationship between the rupture length (L_{rup}), coseismic slip (δ), and T (Supplementary Fig. S6a,b). Because we calculate the rupture area as that of a circular patch of diameter L_{rup}, the moment released is proportional to L_{rup}^2 and because slip scales with L_{rup}, moment scales as duration cubed. Further, the average rupture velocity (v_{rup}) is apparently independent of M although the events exhibit a moment dependent variation in stress drops (Supplementary Fig. S6c,d). This further supports our explanation of these complex events, i.e., arising due to elastic interactions and associated prestress heterogeneities rather than different frictional/mechanical processes (*18*).

Our results suggest that the linear scaling of $M \propto T$ could be an artefact (*52*) of combining different slow slip modes (such as SSE, Episodic Tremor and Slip – ETS, VLF, LFEs etc.) from plate interfaces around the world, and that the spectrum of tectonic slip modes likely follows similar frictional mechanics. Further, geological studies show that shear band thickness scales directly with the mean grain size in granular shear zones, with the scaling factor being dependent on initial grain size distribution (*20,53*). Therefore, the apparent linear scaling of $M \propto T$ could additionally be due to the direct relationship between shear zone thickness, grain size, and Dc. Alternatively, the linear scaling between M and T could represent an upper bound on the speed of slow earthquake modes which are thought to propagate via stress diffusion, i.e., local or nearest-neighbor stress interactions (*54*) which are well-captured by our numerical models.

A spectrum of tectonic slip modes at different scales

Both slow and fast earthquakes have been observed to occur (spatially co-located) on the same fault (*7,45,55*). Our lab experiments and numerical models provide an explanation for such observations. We show that even in the absence of externally imposed or geometric heterogeneities, some combination of self-generated stress heterogeneities over multiple earthquakes, variations in the degree of slip localization, and slip localization at multiple scales within the fault zone are sufficient to reproduce these slow slip modes on the same fault (Fig. 4b). If one follows a line of constant H/L_c (or H/Dc) from the widest to the narrowest fault (Fig. 4b) with progressively increasing background strain rates, we find a family of slow earthquakes (pathway I in Fig. 4b), i.e., SSEs on the wider shear zone, LFEs and VLFEs on the narrower more localized shear zones (Fig. 4c). Physically, this represents a hierarchy of complexities at different scales in fault zones, i.e., families of narrower shear zones that act independently or in a coordinated fashion through anastomosing, geometrically complex interactions (*7,8,27,28,29,56*) within a wider fault zone. The zone of active shear is likely strain rate dependent, thus faults with wider zones of active shear may localize strain in a different way than rougher, narrower fault zones to produce families of faults that are self-similar (Fig. 4c). However, not all fault zones host slow earthquakes at the same depth range – for example, slow slip occurs at shallow depths on the northern end of the creeping section of the San Andreas (*52*), and others such as the locked, shallow portion of the Cascadia margin may exclusively be home to infrequent dynamic ruptures (*57*). Still others, such as the northern Hikurangi margin are home to SSEs and microseismicity but no detectable LFEs, VLFEs or tremors

(*58*). In the laboratory, such hierarchical, multi-level degrees of complexity in rupture behaviors have been reported extensively, usually in the form of slow stick-slip instabilities at the centimeter scale and acoustic emissions at the micro- to nanometer scales (*8* and references therein).

The framework proposed here allows the existence of all these scenarios because the only intrinsic assumption is that Dc (and by proxy L_c) encodes information about strain localization such that H/L_c is of order 1. If the critical patch size, L_c, becomes larger than fault zone width, H, for progressively smaller faults within a main fault zone, it may be energetically unfavorable for the nucleation of tremorgenic slow earthquakes (pathway ii in Fig. 4b). This scenario produces km-scale SSEs with no associated LFEs or VLFEs on smaller fractures. This would physically represent a fault zone where deformation is distributed at the smaller scales with few or no mature, well-localized fault strands. Conversely, if L_c reduces faster than H for smaller faults (pathway iii in Fig. 4b), the main fault zone may creep or host long-term SSEs, and thinner fractures may host microseismic events or infrequent dynamic earthquakes. Physically, this implies that the dynamic ruptures and microseismicity may be accommodated on mature and well-developed slip planes within the fault zone and the slow transients (and SSEs) are accommodated across the entire fault zone thickness (e.g., *28*).

Additionally, our choice of constant H/Lc is computationally convenient and faults in nature may not be as well-behaved. In reality, Lc likely enjoys a highly non-linear relationship with the zone of active shear deformation (solid grey curve in Fig. 4b) but the general spirit of our framework remains unchanged. Moreover, although we modulate L_c in our suite of simulations by changing Dc, other mechanical and frictional properties could also affect H/L_c. In nature, these variations in H/L_c could occur in space and/or time. For example, seamount subduction is likely to cause stress heterogeneities with higher-than-expected normal stress downdip and stress shadows updip of the seamount (*59*). Dc increases with effective stress (*1,2*) and L_c is inversely related to effective stress, which may vary H/L_c along the subduction plate interface and affect the scale-dependence of slip behavior (pathway i, ii, iii or some combination thereof in Fig. 4b) at different locations along the plate interface. We also note that in our simulations, the different fault length scales exist separately and there are no explicit spatial or temporal feedbacks between the different length scales. Future studies that expressly simulate ruptures in a complex fault zone containing anastomosing structures over numerous length scales (Fig. 4c and the synoptic view presented by ref. *28* in their Fig. 6) may provide additional insights into how active fault structures interact over different length and time-scales.

Phase space responses similar to that documented in Fig. 4b have been observed in elastic half-space models of earthquake rupture (*16,60*) where the bifurcation between creep and fast seismic events is controlled by the ratio of the fault dimension along shear slip and the critical nucleation dimension. However, in our models a shear zone thickness (H) which modulates loading behavior is explicitly incorporated. This implies that the competition between loading and RSF, i.e., H/Lc, controls the range of observed slip behaviors (*15*) and provides a direct connection to the strain rates, slip modes, and associated shear structures observed in crustal fault zones.

Lithological and structural heterogeneities have been documented in exhumed faults associated with SSE hosting subduction settings (*28,61*), and through direct observations of shallow SSE source material (*7*). Moreover, field geological observations (*7*) (Fig. 4d), frictional studies (*25*) and numerical models (*62,63*) indicate that brittle failure of competent lenses in a ductile matrix of weak phases are especially conducive to the generation of both shallow and deep SSEs and slow creep transients. How this related to other slow earthquake modes such as LFEs and VLFEs remains an open question. Within the broad slow earthquake fault zone structure, tremors, LFEs and VLFEs could result from the brittle breakage of competent lenses (*64*) while well-developed slip zones extending for many kilometers may accommodate dynamic ruptures (*28*). Ultimately, the presence of heterogeneities and structural complexities at all scales (Fig. 4b,c,d) is captured in our framework through a careful consideration of tectonic strain rates and the quantity

H/L_c (Fig. 4a). Individual faults/fractures with a broad range in the degree of localization and compliance make up natural fault zones, and this diversity in fault maturity can allow a range of tectonic slip styles at different scales. Taken together, our laboratory and numerical models imply that the same fault zone or 'patch' may be capable of hosting complex slip behaviors including slow and fast slip without explicit requiring external heterogeneities. However, such heterogeneities likely enhance complexities observed in nature and allow these complexities to be sustained over a broad range of geological conditions (*5*,*6,7,8,18,65*).

Methods

Friction experiment:

The laboratory friction experiments were performed in a biaxial testing apparatus at Penn State. In this setup, a packed layer of quartz powder (Min-U-Sil 40, US Silica) with mean particle size of 10 μm was sandwiched between two grooved steel forcing blocks (Fig. 1a). The smaller, fixed block had a nominal contact surface area of 5 x 5 cm^2 and this area was kept constant for the duration of the experiment. A servo-hydraulic piston applied a fault normal stress (21 MPa). A second servo-hydraulic piston applied a constant velocity (4.3 or 12.9 μm/s) to the longer (moving) block to shear the simulated fault zone. The moving block slid against a mirror-smooth steel block further lubricated with Molykote grease. Our calibration experiments show that the lubricated surface has friction < 0.01, thus all of the frictional variations reported here are for the quartz gouge. The apparatus was destiffened by means of an acrylic spring in series with the shear load so that frictional stick-slip instabilities could be observed (*44*). Experiments were carried out at room temperature (24 ^{0}C) under 100% relative humidity to ensure reproducibility.

During an experiment, normal stress, normal displacement, shear stress and load-point displacement were continuously measured at 10 kHz and averaged to 1 kHz for storage. Stresses were measured using calibrated full-bridge strain gauge load cells (resolution of ±5 N) and displacements were measured at the load point, i.e., at the piston rather than at the sample, using direct current linear variable differential transformers (DC-LVDT) with a resolution of ±0.1 μm. Initially, the sample was sheared at 12.9 μm/s for 10 mm, and the shear stress was fully unloaded and reloaded to promote creation of the shear fabric that yields steady state shear and to measure the loading stiffness (k) for the experiment. Subsequently, the fault was sheared at 12.9 μm/s for ~43 mm and at 4.3 μm/s for the remaining displacement (Supplementary Fig. S7).

Because we did not have a direct measurement across the fault, we determined fault slip by approximating the configuration as a 1-dimensional spring-block slider. Then,

$$\dot{\tau} = k\left(V_{lp} - V_{slip}\right) \quad (1)$$

Here, $\dot{\tau}$ is the rate of change of shear stress with time, V_{lp} is the load-point velocity and V_{slip} is the fault slip rate. Fault slip, δ_{slip}, in this framework, is the integration of V_{slip} over time. Stiffness, k, for a stick-slip instability is the slope of the linear portion of the increasing shear stress per unit displacement (Supplementary Fig. S8). We calculate the amount of slip for a single stick-slip instability during the friction experiment as the slip experienced between peak stress at the onset of instability and the minimum stress at the end of the instability (Supplementary Fig. S8).

Numerical model:

Fault gouge momentum conservation:

We develop a model to understand spatiotemporal variations in shear displacement over a fault zone of finite thickness (Fig. 1). We treat the gouge as an elastic media of shear modulus G,

length L and thickness H. The model is inspired by the continuum version of the Burridge-Knopoff model (*39*) and the continuum fault zone model of (*15*).

Our model is driven by a constant driving velocity, u_0 at the top and bounded at $z = H$ by a frictional surface that obeys a single-state variable rate-and-state friction constitutive equation with the Aging (Dieterich) law for state evolution (*1,2,60*) (Fig. 1b). We solve the force balance using the Fast Lagrangian Analysis of Continua (FLAC) algorithm (*14*,*63,66,67*). We study the case where shear displacements in the x-direction vary linearly with depth z. We do not consider compaction or dilation of the material so displacements in the z-direction are only those due to elastic deformation within the fault zone. Displacements within the fault zone vary with position and time and are given by:

$$u(x,z,t) = u_0 + \frac{z}{H}(u(x,H,t) - u_0). \quad (2)$$

where u_0 is the loading velocity and $u(x,H,t)$ is determined by the balance of elastic and frictional forces at $z = H$. Frictional resistance on surfaces internal to the layer are not considered. The surface at $z = H$ obeys rate and state friction (*21,22,68*). Each point on the fault surface at x_i moves with velocity V_i in the x-direction. The fault zone is two dimensional and discretized in the x-direction into a grid of equidistant nodes that are spaced Δx distance apart. We do not consider out of plane forces or displacements. We consider horizontal (shear) deformation in the x-direction for adjacent points x_+ and x_- which results in a shear stress, σ_{zx}, between the two points x_+ and x_- in the gouge as:

$$\sigma_{zx}(x,z,t) = G\left(\frac{u_x(x,z,t) - u_0}{z}\right) + \frac{E}{2}(\epsilon(x_+,z,t) - \epsilon(x_-,z,t)) \quad (3)$$

In equation (3), $\epsilon(x_+,z,t)$ and $\epsilon(x_+,z,t)$ represent the elastic strains induced in the fault surface at x_i due to neighboring points at x_{i-1} and x_{i+1} respectively, and E is the Young's modulus of the fault gouge. To determine time variations in position and velocity due to the elastic interactions within the fault gouge, we must conserve momentum and balance the forces caused by differential shear motion of each elastic particle within the fault gouge using Newton's law (Fig. 1b). We write Newton's law in the fault gouge as the wave equation over the thickness of the gouge:

$$\int_0^H G\frac{\partial^2 u(x,z,t)}{\partial x^2}dz = \int_0^H \rho\frac{\partial^2 u(x,z,t)}{\partial t^2}dz \quad (4)$$

ρ is the density of the material in the layer. Since the displacement varies linearly with depth within the fault according to equation (2) we can write:

$$\int_0^H G\frac{z}{H}\frac{\partial^2 u(x,H,t)}{\partial x^2}dz = \int_0^H \rho\frac{z}{H}\frac{\partial^2 u(x,z,t)}{\partial t^2}dz \quad (5)$$

Integrating over z, we obtain a statement about the propagation of displacements in the fault gouge:

$$G\frac{\partial^2 u(x,H,t)}{\partial x^2} = \rho\frac{\partial^2 u(x,H,t)}{\partial t^2} \quad (6)$$

Note that G/ρ has the dimensions of *Length*^{2} *x Time*$^{-2}$ and thus taking the square root yields dimensions of velocity *Length x Time*$^{-1}$, which we call $C_s = \sqrt{G/\rho}$. This corresponds to the maximum shear wave speed in the fault zone. We therefore solve the following boundary value problem:

$$\frac{\partial^2 u(x,H,t)}{\partial x^2} = \frac{1}{C_s^2}\frac{\partial^2 u(x,H,t)}{\partial t^2} \quad (7)$$

Substituting $u(x,0,t) = u_0$, $\frac{\partial u(0,H,t)}{\partial x} = 0$, $\frac{\partial u(L,H,t)}{\partial x} = 0$ and a rate and state surface at H, variations in shear stress at the bottom boundary are due to the interactions between the elastic behavior of the gouge and the frictional behavior of the bottom boundary. To satisfy the bottom boundary condition, for each element we evaluate $V(x,H,t)$. The unknown $V(x,H,t) \equiv V_H(x,t)$ is the slip velocity at the base boundary of the fault zone generated by the traction balance between

variations in elastic shear stresses $\sigma_{zx}(x,H,t) = \tau_0$ of the fault gouge elements according to equation (7), the elastic loading of each element the fault gouge, $\Delta\tau_{load}$ for loading velocity V_0, the rate-state frictional stress at the base of the fault, τ_{rs}, and radiation damping, τ_{rd} (*11,12,13,66,67*). The latest two terms represent forces that oppose motion generated by the stress terms τ_0 and $\Delta\tau_{load}$. The traction balance is written as:

$$\tau_0 + \Delta\tau_{load} - \tau_{rd} - \tau_{rs} = 0 \quad (7)$$

Assuming elastic behavior in the gouge and ignoring Poisson's ratio for convenience ($E \approx 2G$), the shear stress balance can be re-written by combining equations (3) and (7) as:

$$\tau_0 = G(\epsilon_{old} + \frac{\partial u(x,z,t)}{\partial x}) = \tau_{rsf} + \tau_{rd} - \Delta\tau_{load} \quad (8)$$

In equation (8), ϵ_{old} is the accumulated elastic shear strain up to the current time-step and the spatial derivative of shear displacement includes elastic interactions from neighboring nodes in the discretized fault zone grid. In each timestep, the strain history is updated as $\epsilon_{new} = \epsilon_{old} + \frac{1}{2}\frac{(u_0 - u_H(x,t))}{H}$. We can expand and re-write equation (8) explicitly as

$$\tau_0 = G\{\epsilon_{old} + \frac{H}{(\Delta x)^2}(u_H(x+\Delta x,t) + u_H(x-\Delta x,t) - 2u_H(x,t))\} = \tau_{rsf} + \tau_{rd} - \frac{G(u_0 - u_H(x,t))}{H} \quad (9)$$

The friction at the base of the fault gouge is:

$$\tau_{rs} = \sigma_n\left[\mu_r + a\, ln\left(\frac{V_H(x,t)}{V_r}\right) + b\, ln\left(\frac{\theta V_r}{D_c}\right)\right] \quad (10a)$$

$$\frac{d\theta}{dt} = 1 - \frac{\theta V_r}{D_c}, \quad (10b)$$

where μ_r is a reference value of friction at velocity V_r, σ_n is fault normal stress and the parameters a, b, and D_c, are empirically determined in laboratory experiments. Equation 10b describes the evolution of a friction state variable that accounts for memory of past states. The term θ is generally thought of as the lifetime of sliding asperity contacts but it can also represent the porosity within a granular fault zone (*2,20,21,68*). In addition to an explicit frictional shear resistance, we account for energy lost via elastic wave radiation using a radiation damping term (*13*):

$$\tau_{rd} = \frac{G}{2C_s}V_H(x,t) \quad (11)$$

$V_H(x,t)$ and $u_H(x,t)$ are obtained by solving the following equation iteratively using the Raphson-Newton method, since explicitly $u_H(x,t) = V_H(x,t)dt$:

$$G\{\epsilon_{old} + \frac{H}{(\Delta x)^2}(u_H(x+\Delta x,t) + u_H(x-\Delta x,t) - 2u_H(x,t))\} + \frac{G(u_0 - u_H(x,t))}{H} - \sigma_n\left[\mu_r + a\, ln\left(\frac{V_H(x,t)}{V_r}\right) + b\, ln\left(\frac{\theta V_r}{D_c}\right)\right] - \frac{G}{2C_s}V_H(x,t) = 0 \quad (12)$$

Fault gouge constitutive update and numerical scheme:

We determine the slip velocity at the base of the fault zone using Equation (12). The displacement profile as a function of depth z in the fault gouge is then obtained using Equation (2) and the shear stress σ_{zx} is updated explicitly. Once the stress on the friction surface is updated, we solve for elastic interactions within the layer as a function of position and time $u(x,z,t)$ using Equation (8).

For application to the laboratory experiments in our study, where slip velocities are slow and accelerations are small, we use a quasi-dynamic solution of Equation 7 (*13*). We solve Equation

7 using a Lagrangian formulation with a dynamic relaxation method (*14*,*63,66,67*). Our method uses a quasi-dynamic solution of the wave equation as a damped wave propagation problem for Equation 7. We solve the problem on a mesh that discretizes the fault gouge (Fig. 1b). Stresses and displacements are updated using time steps according to a displacement function $u(x,z,t)$ and Equations 9-12.

Because the deformation is linear-elastic in z, the displacement at every point (x, z, t) within the fault zone is given by Equation (2). The non-linear nature of the rate and state formulation for friction imposes the use of very small timesteps (*13*) and explicit numerical methods that are better suited to solve a non-linear wave propagation problem. To simplify the numerical formulation and the rate/state friction law, we solve Equation 6 at explicit nodes *i* on the fault surface (Fig. 1b) but still accounting for stress transfer and force balance everywhere within the fault zone. Stresses are transferred within the fault zone according to the wave equation. We solve for frictional displacement at each node *i* by applying Newton's second law for the force F_+ applied between all nodes and explicitly between nodes **i-1**, **i,** and **i+1.** The force balance is applied independently on a staggered grid. To account for the force interaction on both sides of each zone the solution is alternatively propagated forward and backward in space (Fig. 1b). That is, we use both forward and backward propagating solutions:

$$\rho_f \frac{\partial V_\mathbf{i}}{\partial t} = F_+(1 - 0.8sign(V))) \quad \text{and} \quad \rho_f \frac{\partial V}{\partial t} = F_-(1 - 0.8sign(V)) \tag{13}$$

For clarity we define $V_x := V$ and $\tau := \sigma_{zx}$ and $F_+ = \frac{\tau_{\mathbf{i+1}} - \tau_\mathbf{i}}{|x_{\mathbf{i+1}} - x_\mathbf{i}|}$ and $F_- = \frac{\tau_{\mathbf{i-1}} - \tau_\mathbf{i}}{|x_{\mathbf{i-1}} - x_\mathbf{i}|}$ with $x_\mathbf{i} = \frac{1}{2}(x_i + x_{i+1})$ and similarly for $x_{\mathbf{i+1}}$ and $x_{\mathbf{i+1}}$. The resulting alternate direction numerical scheme is the following. To estimate the contribution of the force in the forward direction:

For $\mathbf{i} = 2, \dots, N$

$$V_\mathbf{i}(t + dt) = V_\mathbf{i}(t) + \frac{\Delta t}{\rho_f} \frac{\tau_{\mathbf{i-1}} - \tau_\mathbf{i}}{|x_{\mathbf{i+1}} - x_\mathbf{i}|} \left(1 - 0.8sign\left(V_\mathbf{i}(t)\right)\right) \tag{14a}$$

To estimate the contribution of the force in the backward direction:

For $\mathbf{i} = N, N-1, \dots, 2$

$$V_\mathbf{i}(t + dt) = V_\mathbf{i}(t) + \frac{\Delta t}{\rho_f} \frac{\tau_{\mathbf{i-1}} - \tau_\mathbf{i}}{|x_{\mathbf{i+1}} - x_\mathbf{i}|} \left(1 - 0.8sign\left(V_\mathbf{i}(t)\right)\right) \tag{14b}$$

The velocities at each node are then computed as $V_i = \frac{1}{2}(V_\mathbf{i} + V_{\mathbf{i+1}})$ and the model node positions are updated as $x_i = x_i + V_i \mathrm{dt}$ to account for elastic deformation.

Consistency and stability of numerical scheme:

If we omit the radiation damping term of Equations 8 and 11, for clarity, the explicit numerical scheme of Equation 14 can be rewritten as:

$$\rho_f \frac{\partial V_\mathbf{i}}{\partial t} = F_+ - F_- \tag{15}$$

We can rewrite the velocity and forces in the elements as a function of displacement with $\tau_\mathbf{i} = \frac{G}{H} \frac{\partial u_i}{\partial x}$, $F = \frac{\partial \tau_\mathbf{i}}{\partial x}$ and $V_\mathbf{i} = \frac{\partial u_i}{\partial t}$. For simplicity of description (note that we solve the problem on a staggered grid for improved resolution) we can describe this using a constant grid space Δx:

$$\rho_f \frac{\partial^2 u_i}{\partial t^2} = \frac{\tau_{\mathbf{i+1}} - \tau_\mathbf{i}}{\Delta x} - \frac{\tau_{\mathbf{i-1}} - \tau_\mathbf{i}}{\Delta x} \tag{16}$$

$$\rho_f \frac{\partial^2 u_i}{\partial t^2} = \frac{\tau_{i+1} - \tau_{i-1}}{\Delta x} = G\left[\frac{1}{\Delta x}\left[\frac{u_{i+1} - u_i}{\Delta x} - \frac{u_i - u_{i-1}}{\Delta x}\right]\right] \quad (17)$$

$$\rho_f \frac{\partial^2 u_i}{\partial t^2} = G\left[\frac{u_{i+1} - 2u_i + u_{i-1}}{\Delta x^2}\right] \quad (18)$$

As $\Delta x \to 0$

$$\rho_f \frac{\partial^2 u_i}{\partial t^2} = G\frac{\partial^2 u_i}{\partial x^2} \quad (19)$$

Our numerical scheme is consistent with Equation 7. Stability is guaranteed by adaptive time stepping following the Courant-Friedrichs-Lewy (CFL) condition (*13,69*). The damping term to critically reach quasistatic equilibrium is given as a damping force (*66*). In our solutions the damping force is always small and on the order of up to tens of Pascals. Since the algorithm is designed to provide the quasi-dynamic solution, the fictitious mass can be viewed as a set of relaxation factors and these can be adjusted to optimize the speed of convergence (*66*). In our formulation the time step is set by the maximum slip rate following *13*:

$$\Delta t = \frac{1}{5}\frac{D_c}{V_s^{max}} \quad (20)$$

where $V_s^{max} = \max\left(V_s(x,t)\right)$. Assuming $V_s^{max} = \sqrt{G/\rho_f}$, where G is Shear modulus for the fault gouge, we can optimize the time step using the fictitious density given by:

$$\rho_f = \frac{G}{(V_s^{max} dx_{min}/D_c)^2} \quad (21)$$

where dx_{min} is the smallest grid size at time t. We limit the slip velocity to the shear velocity C_s. In that case the time step becomes:

$$\Delta t = \frac{1}{5}\frac{dx_{min}}{C_s} \quad (22)$$

and the fictitious density is:

$$\rho_f = \frac{G}{C_S^2} \quad (23)$$

The resulting numerical scheme is stable using the dynamic time stepping scheme described above (68), therefore it is convergent. Dissipation occurs in cases where inertial effects are dominant since the scheme is second order.

<u>*Special case of the laboratory experiments:*</u>

For the laboratory experiment described in our study, elastic strain is experienced by the loading system as a combination of both shear strain accumulation in the fault zone and compressional strain in the elastic spring (PMMA) used in series with the vertical loading ram (Fig. 1a). That is, $\varepsilon_{pmma} = \frac{\tau_{elastic}}{G_p}$, $\varepsilon_{gouge} = \frac{\tau_{elastic}}{G}$ and $2\tau_{elastic} = G_p\varepsilon_{pmma} + G\varepsilon_{gouge}$, G_p and L_p being the elastic modulus and the length of the PMMA spring, respectively. The stresses can be treated in an additive sense here as the areas associated with force transmission, i.e, the cross-sectional area of the elastic spring and the nominal contact area of the fault zone being sheared are equal (25 cm^2). Therefore, we have:

$$\tau_{elastic} = \frac{1}{2}\left\{\frac{G_p(u_{load} - u_0)}{L_p} + \frac{G_p(V_{load} - V_0)\mathrm{d}t}{L_p} + \frac{G(\bar{u}_H(x,t) - u_0)}{H} + + \frac{G(\bar{V}_H(x,t) - V_{load})\mathrm{d}t}{H}\right\} \quad (24)$$

where u_0 is the load point displacement of the loading system, and u_{load} is the displacement associated with the PMMA spring. If the spring is fully coupled with the rigid shearing plate, u_{load}

corresponds to the displacement of the 1st node in the mesh, $u_{load} = u_1$. The constitutive update becomes:

$$\frac{1}{2}\left\{\frac{G_p(u_{load}-u_0)}{L_p} + \frac{G_p(V_{load}-V_0)\mathrm{d}t}{L_p} + \frac{G(\bar{u}_H(x,t)-u_0)}{H} + \frac{G(\bar{V}_H(x,t)-V_{load})\mathrm{d}t}{H}\right\} - \tau_{rd} - \tau_{rd} = 0 \quad (25)$$

After obtaining $V_H(x,t)$, we can explicitly update the fault gouge momentum balance using Equation 12, substituting $\left[\frac{G}{H}\left(u_0 - u_H(x,t)\right)dt\right]$ by $\left[\frac{G_p(V_0-V_{load})\mathrm{d}t}{L_p} + \frac{G(V_{load}-\bar{V}_H(x,t))\mathrm{d}t}{H}\right]$.

A fault patch can only nucleate an instability (earthquake, slow transient etc.) if the size of the frictionally unstable (velocity-weakening) portion of the fault patch exceeds a critical nucleation length, L_c, given by (*71*)

$$L_c = \frac{GD_c}{\sigma_n(b-a)_{max}} \quad (26)$$

The model resolution is governed by the cell/element size, Δx, which is usually selected such that the critical nucleation length, L_c (or sometimes referred to as h^*) and the cohesive zone, Λ_0, are resolved by at least 3 elements (*13*). The cohesive zone, Λ_0, is estimated for our fault as

$$\Lambda_0 = \frac{9\pi}{32}\frac{GD_c}{b\sigma_n} \quad (27)$$

For all of our simulations, the critical nucleation length (L_c) and cohesive zone (Λ_0) are resolved by at least 3 FLAC grid elements to ensure that our model represents a continuum system and that the complex ruptures are not a product of insufficient mesh resolution (*72*).

Estimation of rupture properties in the numerical model:

Our numerical model accounts for the spatiotemporal evolution of fault slip in our lab experiment. In particular, we resolve spatial variations in fault slip over the lab seismic cycle that are not described by the rigid-block, spring-slider model typically assumed in friction experiments. We estimate rupture properties such as average slip ($\bar{\delta}$), rupture area (A), rupture duration (t_{r_d}), maximum slip rate (v_{max}) and average stress drop ($\Delta\bar{\tau}$) for a given slip transient (slow or fast) in our numerical model based on the space-time evolution of mechanical and frictional properties. First, we identify a rupture as a minimum of two cells where the space-time evolution of slip velocity exceeds the background loading rate, i.e., $v_{(i,t)} > v_p$, where i and t represent the mesh element label and time respectively. In this study, we only consider confined ruptures and do not estimate the properties of partially confined or fault-spanning events. Confined ruptures in this context satisfy the criteria $1 < i < N$ and $t_{spin-up} < t < t_{end}$ where $t_{spin-up}$ is the amount of time required for the initial loading and model spin-up, and t_{end} is the simulation end time. Then, the average slip, $\bar{\delta}$, associated with a rupture/event is

$$\bar{\delta} = \frac{\sum \delta_{i,t}}{NI_{rup}} \quad (28)$$

where $\delta_{i,t}$ is the slip in any space-time cell, and N_{rup} is the total number of space-time cells associated with a rupture.

The rupture area, A, is calculated from the rupture length assuming a circular rupture patch in our 1-D fault model. The rupture length is calculated as the maximum distance that the rupture has propagated, and this value is used as the rupture patch diameter to calculate A. The rupture

595 duration, t_{r_d}, is similarly calculated as the total time for which a portion of the fault has experienced elevated slip rates during a rupture. The maximum slip rate, v_{max}, for a rupture is the highest slip rate experienced by any space-time cell during the rupture.

We calculate the average stress drop, $\Delta\bar{\tau}$, as the difference between the maximum and minimum values of spatially averaged stress, over time. In other words,

600 $$\Delta\bar{\tau} = max\left\{\frac{\sum_i \tau}{\sum i}\right\} - min\left\{\frac{\sum_i \tau}{\sum i}\right\} \quad (29)$$

Acknowledgments.
LL was funded by NSF EAR-2121666. CM acknowledges support from the European Research Council Advanced Grant 835012 (TECTONIC) and the RETURN Extended Partnership and funding from the European Union Next-GenerationEU (National Recovery and Resilience Plan – NRRP, Mission 4, Component 2, Investment 1.3 – D.D. 1243 2/8/2022, PE0000005.

Author Contributions. Conceptualization: SS, LL; Lab experiments: SS, CJM; Numerical modeling: SS, LL; Visualization: SS, LL. All authors contributed to the methodology, investigation, funding acquisition, and the writing of the draft manuscript.

Competing Interest. Authors declare that they have no competing interests.

Data/Code Availability. Experimental and simulation data presented here can be downloaded from https://doi.org/10.5281/zenodo.10447872 or by contacting the corresponding author.

References

1. Scholz, C. H. (2019). The mechanics of earthquakes and faulting. Cambridge university press.
2. Marone, C. (1998). Laboratory-derived friction laws and their application to seismic faulting. Annual Review of Earth and Planetary Sciences, 26(1), 643-696.
3. Ruiz, S., Metois, M., Fuenzalida, A., Ruiz, J., Leyton, F., Grandin, R., ... & Campos, J. (2014). Intense foreshocks and a slow slip event preceded the 2014 Iquique M w 8.1 earthquake. *Science*, *345*(6201), 1165-1169.
4. Huang, J., & Turcotte, D. L. (1990). Evidence for chaotic fault interactions in the seismicity of the San Andreas fault and Nankai trough. *Nature*, *348*(6298), 234-236.
5. Yin, Y., Galvez, P., Heimisson, E. R., & Wiemer, S. (2023). The role of three-dimensional fault interactions in creating complex seismic sequences. *Earth and Planetary Science Letters*, *606*, 118056.
6. Romanet, P., Bhat, H. S., Jolivet, R., & Madariaga, R. (2018). Fast and slow slip events emerge due to fault geometrical complexity. *Geophysical Research Letters*, *45*(10), 4809-4819.
7. Barnes, P. M., Wallace, L. M., Saffer, D. M., Bell, R. E., Underwood, M. B., Fagereng, A., ... & IODP Expedition 372 Scientists. (2020). Slow slip source characterized by lithological and geometric heterogeneity. Science Advances, 6(13), eaay3314.
8. Ben-Zion, Y., & Dresen, G. (2022). A synthesis of fracture, friction and damage processes in earthquake rupture zones. *Pure and Applied Geophysics*, *179*(12), 4323-4339.
9. Leeman, J. R., Saffer, D. M., Scuderi, M. M., & Marone, C. (2016). Laboratory observations of slow earthquakes and the spectrum of tectonic fault slip modes. Nature communications, 7(1), 1-6.
10. Shreedharan, S., Bolton, D. C., Rivière, J., & Marone, C. (2020). Preseismic fault creep and elastic wave amplitude precursors scale with lab earthquake magnitude for the continuum of tectonic failure modes. *Geophysical Research Letters*, *47*(8), e2020GL086986.
11. Tse, S. T., & Rice, J. R. (1986). Crustal earthquake instability in relation to the depth variation of frictional slip properties. *Journal of Geophysical Research: Solid Earth*, *91*(B9), 9452-9472.
12. Rice, J. R. (1993). Spatio-temporal complexity of slip on a fault. *Journal of Geophysical Research: Solid Earth*, *98*(B6), 9885-9907.
13. Lapusta, N., & Liu, Y. (2009). Three-dimensional boundary integral modeling of spontaneous earthquake sequences and aseismic slip. Journal of Geophysical Research: Solid Earth, 114(B9).
14. Im, K., & Avouac, J. P. (2021). Tectonic tremor as friction-induced inertial vibration. *Earth and Planetary Science Letters*, *576*, 117238.
15. Horowitz, F. G., & Ruina, A. (1989). Slip patterns in a spatially homogeneous fault model. *Journal of Geophysical Research: Solid Earth*, *94*(B8), 10279-10298.
16. Barbot, S. (2019). Slow-slip, slow earthquakes, period-two cycles, full and partial ruptures, and deterministic chaos in a single asperity fault. *Tectonophysics*, *768*, 228171.
17. Cattania, C. (2019). Complex earthquake sequences on simple faults. *Geophysical Research Letters*, *46*(17-18), 10384-10393.
18. Dal Zilio, L., Lapusta, N., & Avouac, J. P. (2020). Unraveling scaling properties of slow-slip events. Geophysical Research Letters, 47(10), e2020GL087477.
19. Cebry, S. B. L., Ke, C. Y., Shreedharan, S., Marone, C., Kammer, D. S., & McLaskey, G. C. (2022). Creep fronts and complexity in laboratory earthquake sequences illuminate delayed earthquake triggering. *Nature communications*, *13*(1), 6839.
20. Marone, C., & Kilgore, B. (1993). Scaling of the critical slip distance for seismic faulting with shear strain in fault zones. Nature, 362(6421), 618-621.
21. Dieterich, J. H. (1979). Modeling of rock friction: 1. Experimental results and constitutive equations. Journal of Geophysical Research: Solid Earth, 84(B5), 2161-2168.

22. Ruina, A. (1983). Slip instability and state variable friction laws. Journal of Geophysical Research: Solid Earth, 88(B12), 10359-10370.
23. Scholz, C. H. (1988). The critical slip distance for seismic faulting. Nature, 336(6201), 761-763.
24. Scuderi, M. M., Collettini, C., Viti, C., Tinti, E., & Marone, C. (2017). Evolution of shear fabric in granular fault gouge from stable sliding to stick slip and implications for fault slip mode. Geology, 45(8), 731-734.
25. Shreedharan, S., Ikari, M., Wood, C., Saffer, D., Wallace, L., & Marone, C. (2022). Frictional and Lithological Controls on Shallow Slow Slip at the Northern Hikurangi Margin. Geochemistry, Geophysics, Geosystems, 23(2), e2021GC010107.
26. Sleep, N. H. (1995). Frictional heating and the stability of rate and state dependent frictional sliding. *Geophysical research letters*, *22*(20), 2785-2788.
27. Rowe, C. D., Moore, J. C., Remitti, F., & IODP Expedition 343/343T Scientists. (2013). The thickness of subduction plate boundary faults from the seafloor into the seismogenic zone. Geology, 41(9), 991-994.
28. Kirkpatrick, J. D., Fagereng, Å., & Shelly, D. R. (2021). Geological constraints on the mechanisms of slow earthquakes. Nature Reviews Earth & Environment, 2(4), 285-301.
29. Fagereng, Å., & Biggs, J. (2019). New perspectives on 'geological strain rates' calculated from both naturally deformed and actively deforming rocks. Journal of Structural Geology, 125, 100-110.
30. Rabinowicz, E. (1951). The nature of the static and kinetic coefficients of friction. Journal of applied physics, 22(11), 1373-1379.
31. Mclaskey, G. C., & Yamashita, F. (2017). Slow and fast ruptures on a laboratory fault controlled by loading characteristics. Journal of Geophysical Research: Solid Earth, 122(5), 3719-3738.
32. Passelègue, F. X., Schubnel, A., Nielsen, S., Bhat, H. S., Deldicque, D., & Madariaga, R. (2016). Dynamic rupture processes inferred from laboratory microearthquakes. *Journal of Geophysical Research: Solid Earth*, *121*(6), 4343-4365.
33. Gu, J. C., Rice, J. R., Ruina, A. L., & Simon, T. T. (1984). Slip motion and stability of a single degree of freedom elastic system with rate and state dependent friction. Journal of the Mechanics and Physics of Solids, 32(3), 167-196.
34. Mele Veedu, D., Giorgetti, C., Scuderi, M., Barbot, S., Marone, C., & Collettini, C. (2020). Bifurcations at the stability transition of earthquake faulting. Geophysical Research Letters, 47(19), e2020GL087985.
35. Baumberger, T., Heslot, F., & Perrin, B. (1994). Crossover from creep to inertial motion in friction dynamics. Nature, 367(6463), 544-546.
36. Huang, J., & Turcotte, D. L. (1990). Are earthquakes an example of deterministic chaos?. Geophysical Research Letters, 17(3), 223-226.
37. Becker, T. W. (2000). Deterministic chaos in two state-variable friction sliders and the effect of elastic interactions. GEOPHYSICAL MONOGRAPH-AMERICAN GEOPHYSICAL UNION, 120, 5-26.
38. Gualandi, A., Faranda, D., Marone, C., Cocco, M., & Mengaldo, G. (2023). Deterministic and stochastic chaos characterize laboratory earthquakes. *Earth and Planetary Science Letters*, *604*, 117995.
39. Erickson, B. A., Birnir, B., & Lavallée, D. (2011). Periodicity, chaos and localization in a Burridge–Knopoff model of an earthquake with rate-and-state friction. *Geophysical Journal International*, *187*(1), 178-198.
40. Leeman, J. R., Marone, C., & Saffer, D. M. (2018). Frictional mechanics of slow earthquakes. Journal of Geophysical Research: Solid Earth, 123(9), 7931-7949.

41. McLaskey, G. C. (2019). Earthquake initiation from laboratory observations and implications for foreshocks. *Journal of Geophysical Research: Solid Earth*, *124*(12), 12882-12904.
42. Volpe, G., Pozzi, G., Taddeucci, J., Marone, C., & Collettini, C. (2023). Frictional Instabilities in Clay and Implications for Shallow Slow Slips. In *AGU Fall Meeting Abstracts* Vol. 2023.
43. Rowe, C. D., Moore, J. C., Remitti, F., & IODP Expedition 343/343T Scientists. (2013). The thickness of subduction plate boundary faults from the seafloor into the seismogenic zone. *Geology*, *41*(9), 991-994.
44. Shreedharan, S., Bolton, D. C., Rivière, J., & Marone, C. (2021). Competition between preslip and deviatoric stress modulates precursors for laboratory earthquakes. Earth and Planetary Science Letters, 553, 116623.
45. Peng, Z., & Gomberg, J. (2010). An integrated perspective of the continuum between earthquakes and slow-slip phenomena. Nature geoscience, 3(9), 599-607.
46. Tsang, L. L., Meltzner, A. J., Philibosian, B., Hill, E. M., Freymueller, J. T., & Sieh, K. (2015). A 15 year slow-slip event on the Sunda megathrust offshore Sumatra. Geophysical Research Letters, 42(16), 6630-6638.
47. Mallick, R., Meltzner, A. J., Tsang, L. L., Lindsey, E. O., Feng, L., & Hill, E. M. (2021). Long-lived shallow slow-slip events on the Sunda megathrust. Nature Geoscience, 14(5), 327-333.
48. Gomberg, J., Wech, A., Creager, K., Obara, K., & Agnew, D. (2016). Reconsidering earthquake scaling. Geophysical Research Letters, 43(12), 6243-6251.
49. Ide, S., Beroza, G. C., Shelly, D. R., & Uchide, T. (2007). A scaling law for slow earthquakes. Nature, 447(7140), 76-79.
50. Frank, W. B., & Brodsky, E. E. (2019). Daily measurement of slow slip from low-frequency earthquakes is consistent with ordinary earthquake scaling. Science advances, 5(10), eaaw9386.
51. Michel, S., Gualandi, A., & Avouac, J. P. (2019). Similar scaling laws for earthquakes and Cascadia slow-slip events. Nature, 574(7779), 522-526.
52. Tan, Y. J., & Marsan, D. (2020). Connecting a broad spectrum of transient slip on the San Andreas fault. Science advances, 6(33), eabb2489.
53. Rattez, H., Shi, Y., Sac-Morane, A., Klaeyle, T., Mielniczuk, B., & Veveakis, M. (2022). Effect of grain size distribution on the shear band thickness evolution in sand. *Géotechnique*, 72(4), 350-363.
54. Ide, S., & Beroza, G. C. (2023). Slow earthquake scaling reconsidered as a boundary between distinct modes of rupture propagation. *Proceedings of the National Academy of Sciences*, *120*(32), e2222102120.
55. Bürgmann, R. (2018). The geophysics, geology and mechanics of slow fault slip. Earth and Planetary Science Letters, 495, 112-134.
56. Fagereng, Å. (2011). Geology of the seismogenic subduction thrust interface. Geological Society, London, Special Publications, 359(1), 55-76.
57. McGuire, J. J., Collins, J. A., Davis, E., Becker, K., & Heesemann, M. (2018). A lack of dynamic triggering of slow slip and tremor indicates that the shallow Cascadia megathrust offshore Vancouver Island is likely locked. Geophysical research letters, 45(20), 11-095.
58. Wallace, L. M. (2020). Slow slip events in New Zealand. Annual Review of Earth and Planetary Sciences, 48, 175-203.
59. Sun, T., Saffer, D., & Ellis, S. (2020). Mechanical and hydrological effects of seamount subduction on megathrust stress and slip. Nature Geoscience, 13(3), 249-255.
60. Liu, Y., & Rice, J. R. (2007). Spontaneous and triggered aseismic deformation transients in a subduction fault model. Journal of Geophysical Research: Solid Earth, 112(B9).
61. Fagereng, Å. (2011). Geology of the seismogenic subduction thrust interface. Geological Society, London, Special Publications, 359(1), 55-76.

62. Hayman, N. W., & Lavier, L. L. (2014). The geologic record of deep episodic tremor and slip. Geology, 42(3), 195-198.
63. Lavier, L. L., Tong, X., & Biemiller, J. (2021). The Mechanics of Creep, Slow Slip Events, and Earthquakes in Mixed Brittle-Ductile Fault Zones. Journal of Geophysical Research: Solid Earth, 126(2), e2020JB020325.
64. Chestler, S. R., & Creager, K. C. (2017). A model for low-frequency earthquake slip. Geochemistry, Geophysics, Geosystems, 18(12), 4690-4708.
65. Im, K., Saffer, D., Marone, C., & Avouac, J. P. (2020). Slip-rate-dependent friction as a universal mechanism for slow slip events. Nature Geoscience, 13(10), 705-710.
66. Cundall, P. A. (1989). Numerical experiments on localization in frictional materials. Ingenieur-archiv, 59(2), 148-159.
67. Biemiller, J., & Lavier, L. (2017). Earthquake supercycles as part of a spectrum of normal fault slip styles. Journal of Geophysical Research: Solid Earth, 122(4), 3221-3240.
68. Rice, J. R., and Ruina, A. L. (June 1, 1983). "Stability of Steady Frictional Slipping." ASME. *J. Appl. Mech*. June 1983; 50(2): 343–349. https://doi.org/10.1115/1.3167042
69. Lapusta, N., & Rice, J. R. (2000). Elastodynamic analysis of earthquake sequences on slowly loaded faults with rate and state friction. In *2nd ACES Workshop, Japan*.
70. Segall, P., & Rice, J. R. (1995). Dilatancy, compaction, and slip instability of a fluid-infiltrated fault. *Journal of Geophysical Research: Solid Earth*, *100*(B11), 22155-22171.
71. Dieterich, J. H. (1992). Earthquake nucleation on faults with rate-and state-dependent strength. *Tectonophysics*, *211*(1-4), 115-134.
72. Rice, J. R., & Ben-Zion, Y. (1996). Slip complexity in earthquake fault models. *Proceedings of the National Academy of Sciences*, *93*(9), 3811-3818.

Figures and Tables

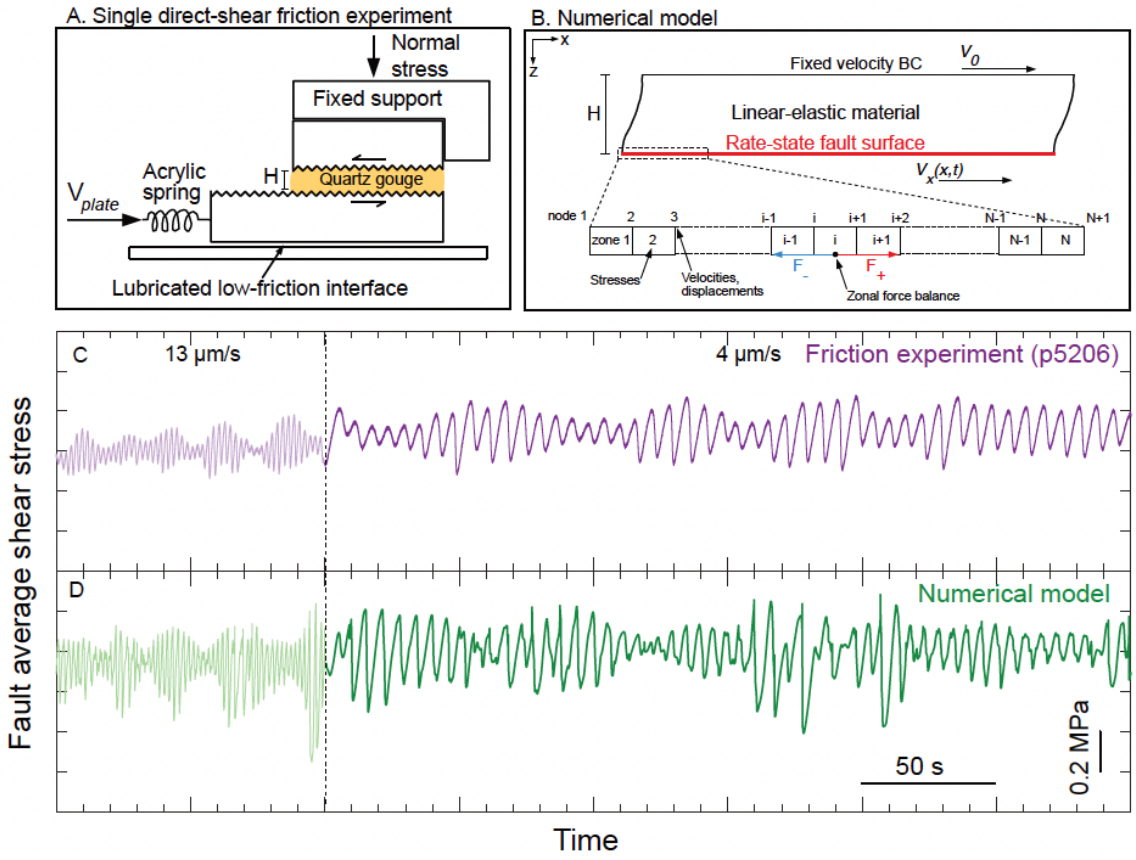

Figure 1. Comparison of numerical model with friction experiment of granular shear. (A) Experimental setup for frictional shear under a constant normal stress. The fault gouge is sheared between two forcing blocks by driving the longer block at a velocity of V_{plate}. **(B)** Numerical model of the friction experiment where the fault zone is represented by a mesh of elastic elements that sit on a fixed substrate. An elastic spring of length L_p and elastic modulus G_p (not pictured) loads the top of the fault zone at (0,0) at a constant background velocity, which in turn loads the slipping interface. At the frictional interface, the elastic loading stresses (τ_e) are balanced by the rate-state frictional stress (τ_{rs}), inter-element force balance, and radiation damping (τ_{rd}). Evolution of the average shear stress in **(C)** the experimental fault and **(D)** in the numerical model for two different driving velocities for normal stress of 21 MPa.

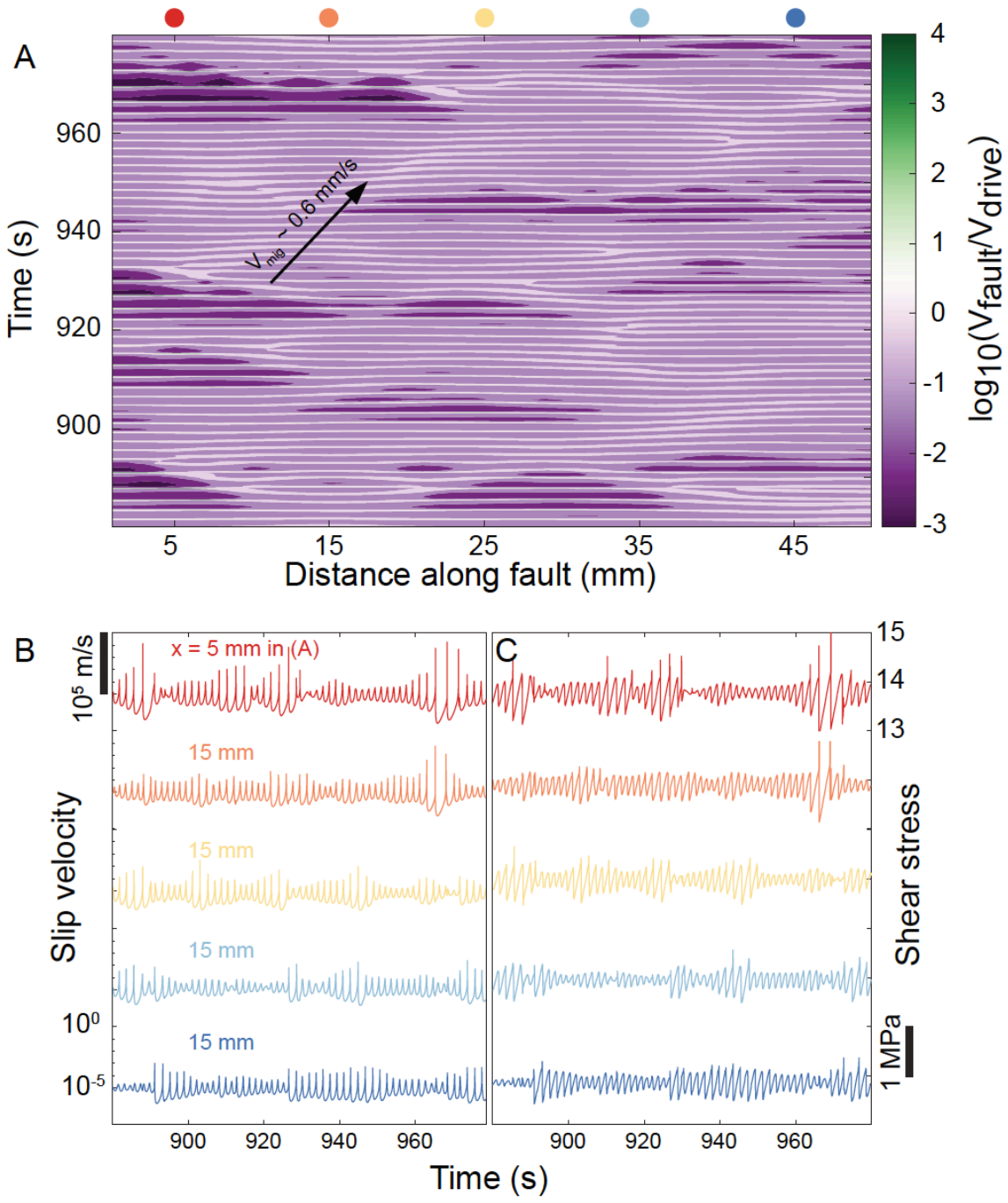

Figure 2. Space-time evolution of earthquakes in the numerical model. (A) Rupture evolution along the fault showing individual slow ruptures migrating in space and time. Deep purples represent locking (slower than driving rate) and deep greens represent coseismic slip (faster than driving rate). The coseismic phase (green) may be more easily seen in Supplementary Fig. S2 which is linear in timesteps (rather than time). Note that slip events nucleate in several places and propagate in both directions. **(B)** Local slip velocity and **(C)** shear stress evolution for several locations (see colored dots in **A**). Note that slip velocity and local stress evolve independently at the locations and show complex evolution of individual slow and fast slip events.

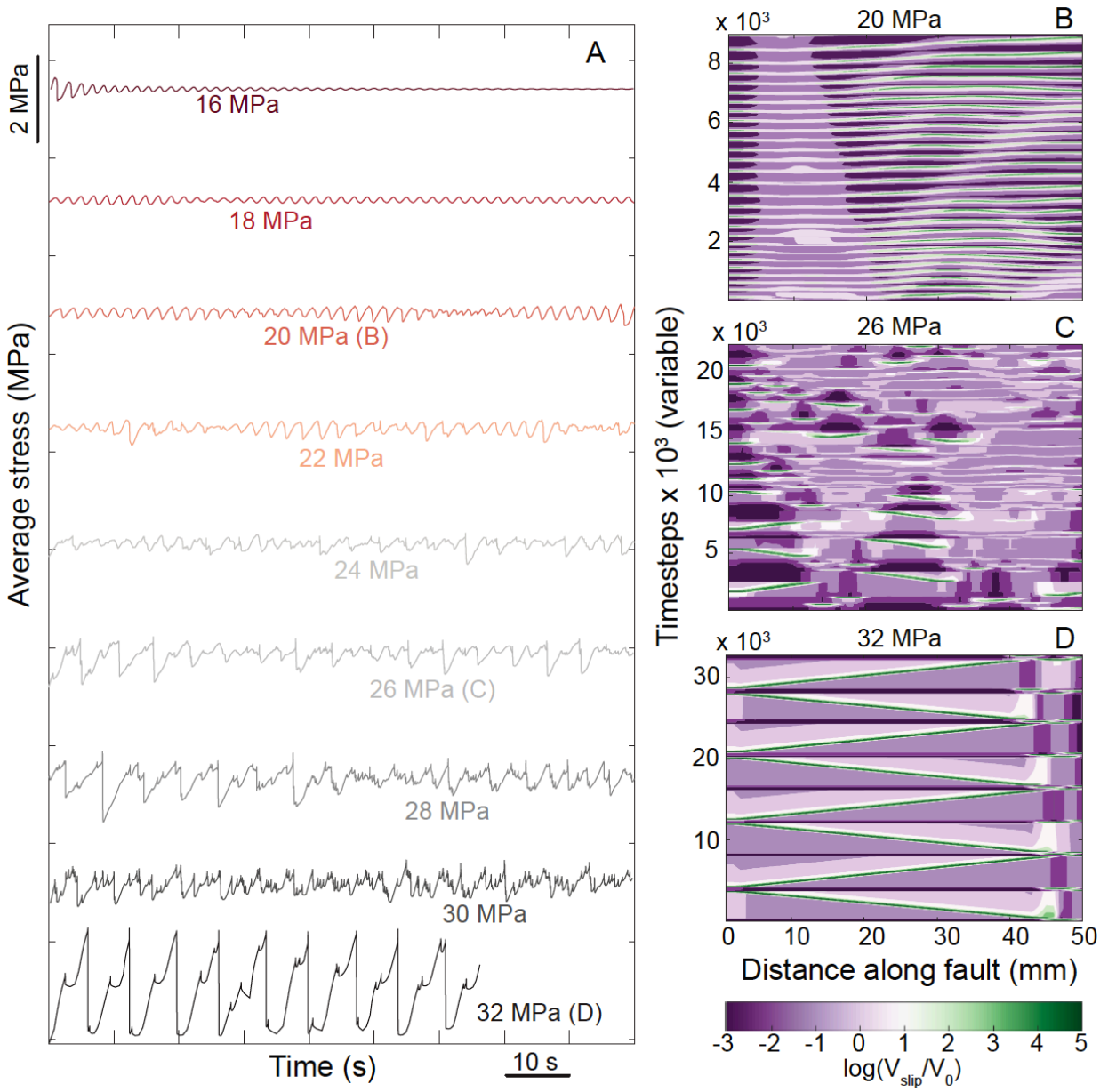

Figure 3. Role of effective normal stress on rupture behavior in the numerical model. (A) Increasing normal stress from 16 MPa to 32 MPa shows progressively more and larger complex ruptures. Space-time(-step) evolution of multiple rupture sequences at **(B)** 20 MPa effective normal stress shows migrating slow ruptures that are either fully or partially confined to the 50 mm fault, **(C)** 26 MPa effective normal stress shows complex sequences of slow and fast ruptures with no discernible migratory trends, and **(D)** 32 MPa effective normal stress shows full-fault ruptures with no clear nucleation, i.e., rigid-block behavior. Deep purple colors in the slip rate contour plots (B-D) indicate locked patches, white color indicates creep at velocities close to background loading rates, and green indicates fast/coseismic slip in space or time.

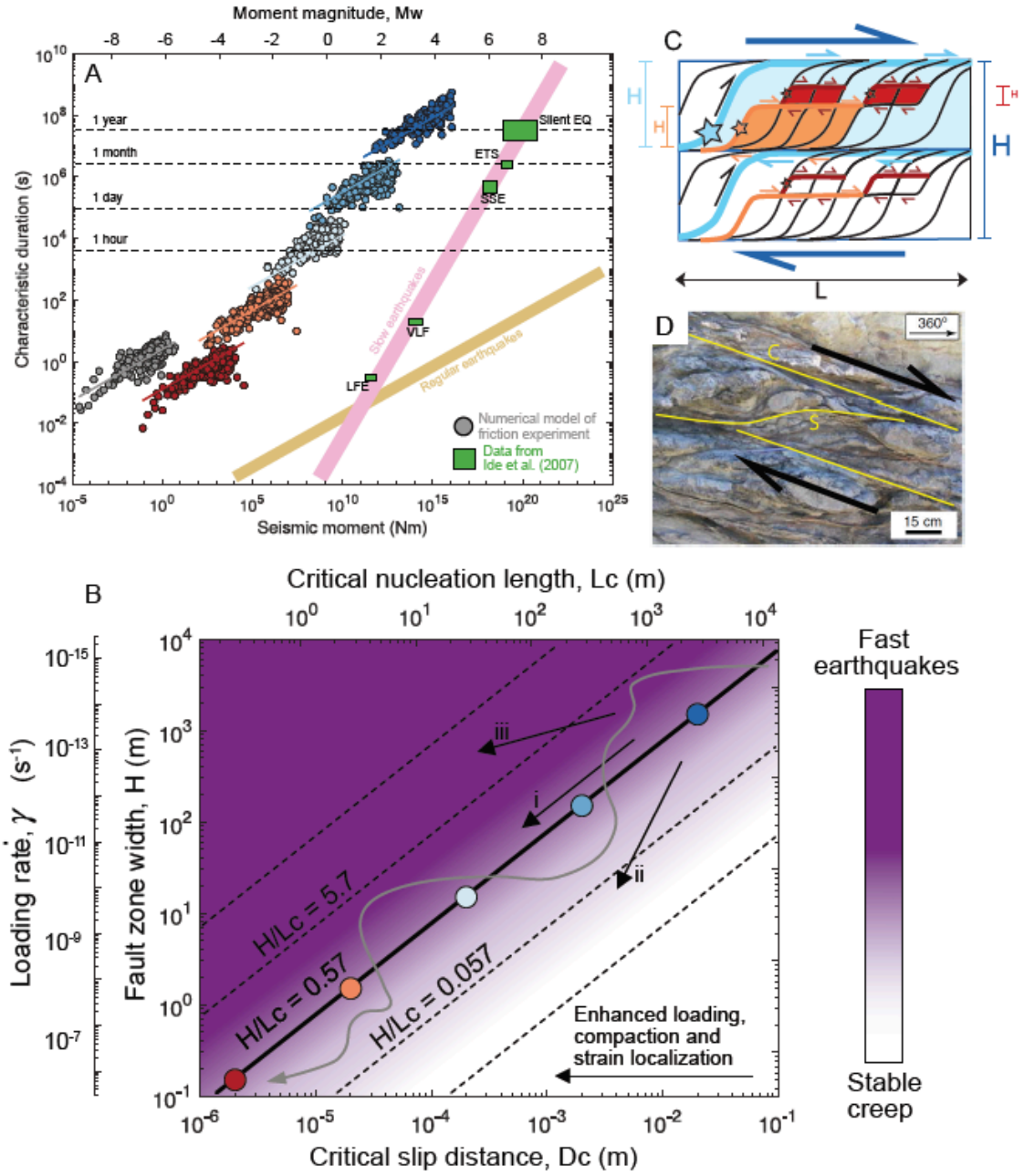

Figure 4. Unifying framework for the spectrum of tectonic slip modes. (A) Characteristic duration, T, increases with magnitude, Mw, as $T^3 \propto M_w$ for families of simulated earthquakes colored by fault zone thickness, Dc and driving velocity. Red to blue lines are cubic fits to the corresponding cluster of circles. Grey cluster represents model results for the parameters of our friction experiments and filled green boxes are values constrained from geophysical measurements of SSEs, LFEs, VLFEs etc. (*49*). Pink and gold regions respectively represent clusters of slow earthquake phenomena ($T \propto M_w$) and regular earthquakes ($T^3 \propto M_w$) populated by (*49*). Our model produces the full spectrum of slip behaviors by assuming that Dc (and by proxy L_c) encodes information about strain localization. **(B)** Relationship between fault zone width, H, and key parameters dictating fault stability and mode of sliding. In our model, H

decreases as shear becomes increasingly localized and the loading fault strain rate, $\dot{\gamma}$, increases. The critical slip distance, *Dc*, decreases with strain localization and this produces families of earthquakes with a particular slip mode from fast to slow. Paths (i), (ii) and (iii), and the grey curve represent relationships between H and L_c as one moves across spatial scales for a range of initial values of fault length, width and Dc. The relevance of these paths are discussed further in the text. Panel **(C)** shows a model fault zone that well represents our suite of 'nested' numerical models where strain is accommodated at different scales and degrees of localization. This produces different styles of instabilities (see Fig. 3). The colors of each suite of numerical models in **(A)**, from red to blue, corresponds to the values of H and Dc used for each model as shown in **(C)**. **(D)** An example from the exhumed Chrystalls Beach Complex where sandstone lenses are embedded in a mudstone matrix. Strain has localized in the matrix and an *S*-*C*-like fabric has developed (*61*).

Supporting Information for

Complex and confined laboratory ruptures explain scaling of the critical slip distance for earthquake faulting

Srisharan Shreedharan[1*], Luc Lavier[2,3] and Chris Marone[4,5]

[1]Department of Geosciences, Utah State University, UT, USA

[2]Institute for Geophysics, Jackson School of Geosciences, University of Texas at Austin, TX, USA

[3]Department of Geological Sciences, Jackson School of Geosciences, University of Texas at Austin, TX, USA

[4]Department of Geosciences, The Pennsylvania State University, PA, USA

[5]Dipartimento di Scienze della Terra, La Sapienza Università di Roma, Italy

*Corresponding author.

Email: srisharan.shreedharan@usu.edu

This PDF file includes:

Figures S1 to S8
Tables S1 to S2
SI References

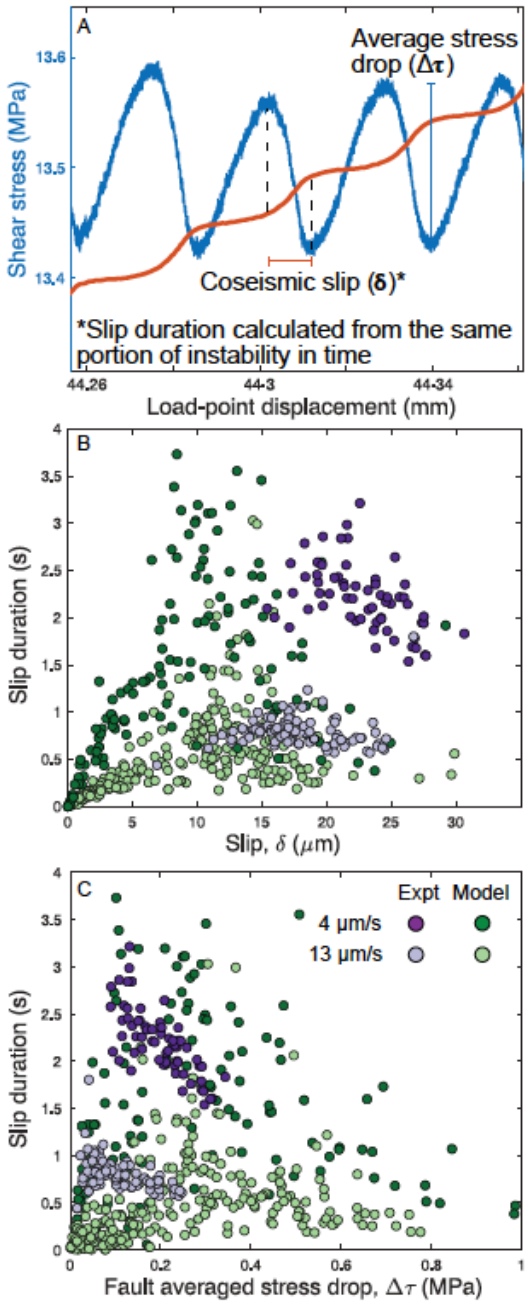

Figure S1. Source properties of ruptures in lab experiments and numerical models. (A) Rupture properties of duration, slip and stress drop. Note that long duration, slow, events have smaller slip and stress drop than short duration, fast events. Panels B and C show slip event duration as a function of fault slip, averaged over the fault surface, and average stress drop. Note that both the lab data (purple) and numerical model results (green) show a complex range of slip event modes ranging from fast to slow with faster events showing larger stress drop and greater fault slip.

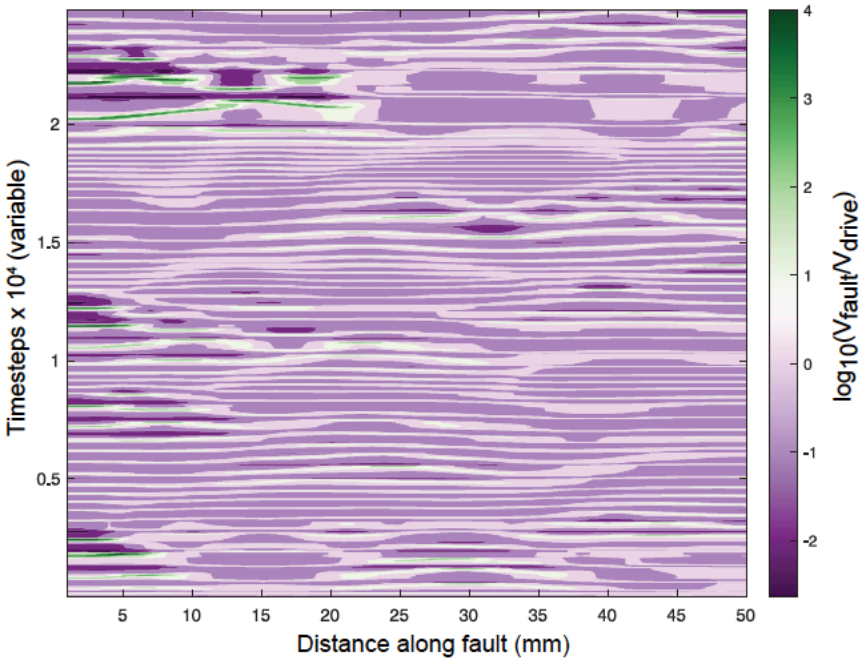

Figure S2. Space-time evolution of ruptures in the numerical model. Each line shows the spatial distribution of fault slip velocity with velocity highlighted by color. Slip events are highlighted by patches of a given velocity (color) that abut locked regions or patches slipping at lower (higher) velocity. Ruptures evolve along the fault over multiple timesteps and show individual slow ruptures migrating in space and time. Fault slip colors use a logarithmic scale defined by the ratio of fault slip rate to background driving rate. Deep purples represent locking (slower than driving rate) and deep greens represent coseismic slip (faster than driving rate).

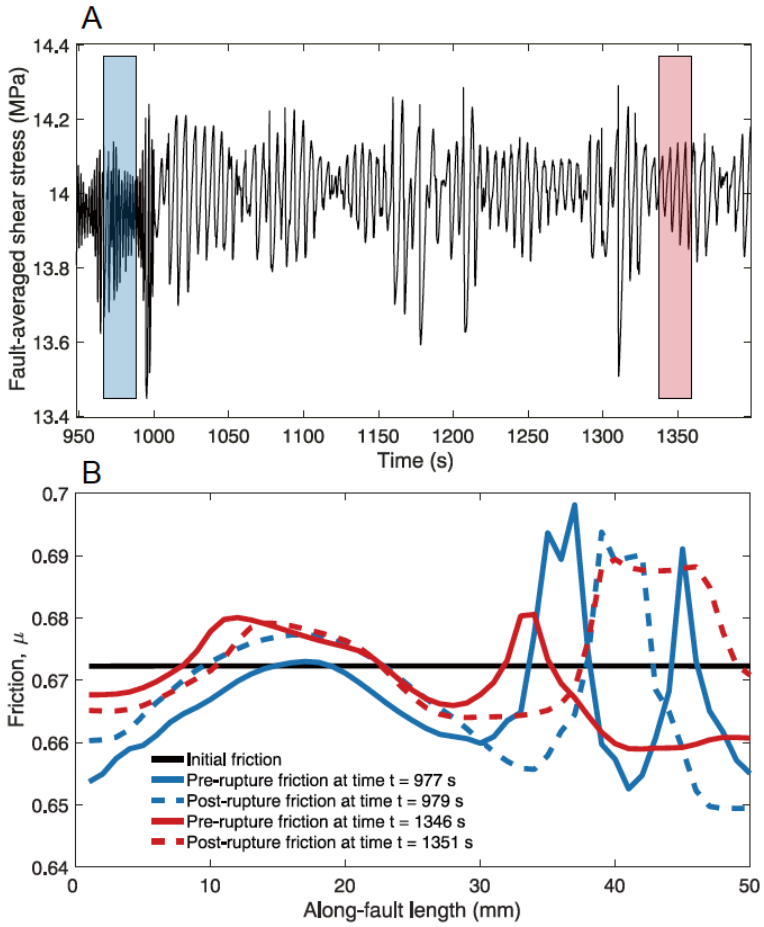

Figure S3. Numerical model results showing shear stress and friction averaged over the fault plane at a fault normal stress of 21 MPa. (A) Note that fault stress and slip event character (see Fig. S1A for event properties of stress drop and duration) exhibit complex aperiodicity including long period modulation of stress drop. (B) Spatial heterogeneity in average fault friction for 5 times ranging from an initial value before slip (black line) to pre/post values for two slip events. The pre- (solid lines) and post-rupture (dashed lines) spatial distribution of friction for driving velocities of 4 μm/s and 13 μm/s are given by the blue and red curves respectively. Colored boxes in (A) show the approximate locations (in time) of the corresponding curves in (B).

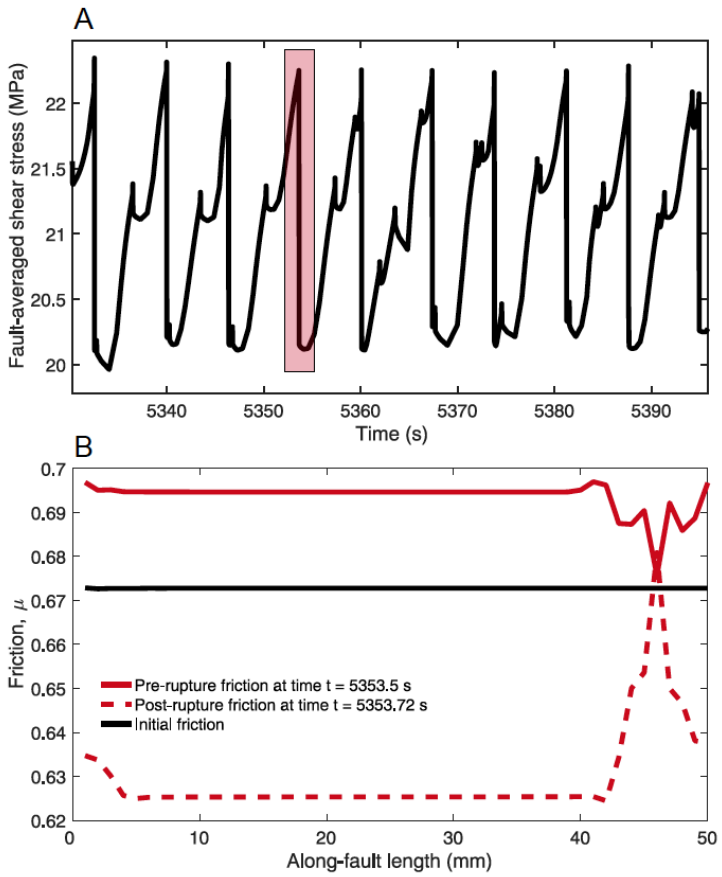

Figure S4. Numerical model results showing shear stress and friction averaged over the fault plane at a fault normal stress of 32 MPa. (A) Evolution of fault-averaged shear stress with time for multiple ruptures in the numerical model and (B) Spatial heterogeneity in shear stress (reported as friction coefficient) immediately before and after a representative fault-spanning rupture. The pre- (solid line) and post-rupture (dashed line) spatial distribution of friction are given by the red curves. Colored box in (A) shows the approximate location (in time) of the corresponding curve in (B).

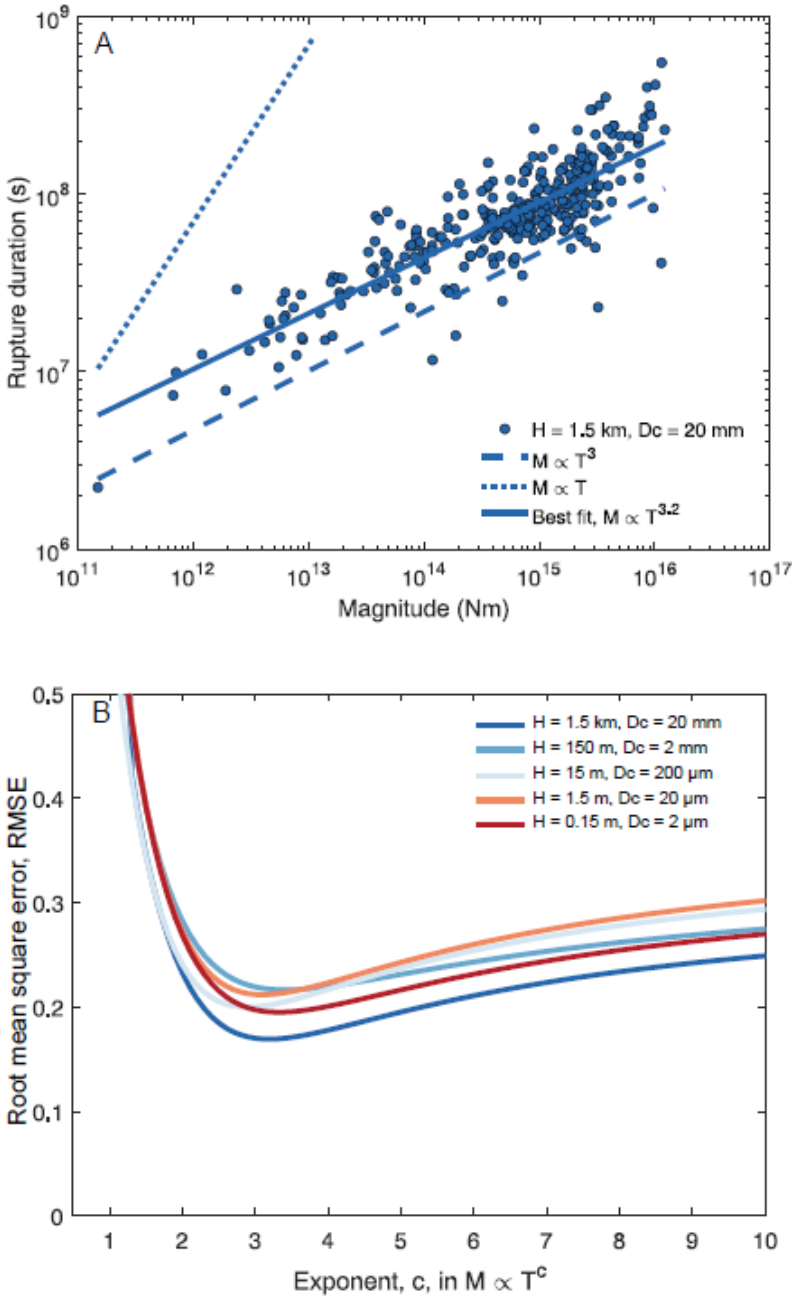

Figure S5. Relationship between seismic moment and characteristic duration. (A) Ruptures in the numerical models are best fit by a relationship described by $M \propto T^{3.2}$ although **(B)** the root mean square error (RMSE) is not significantly different for exponents in the range of 2.5 – 3.5.

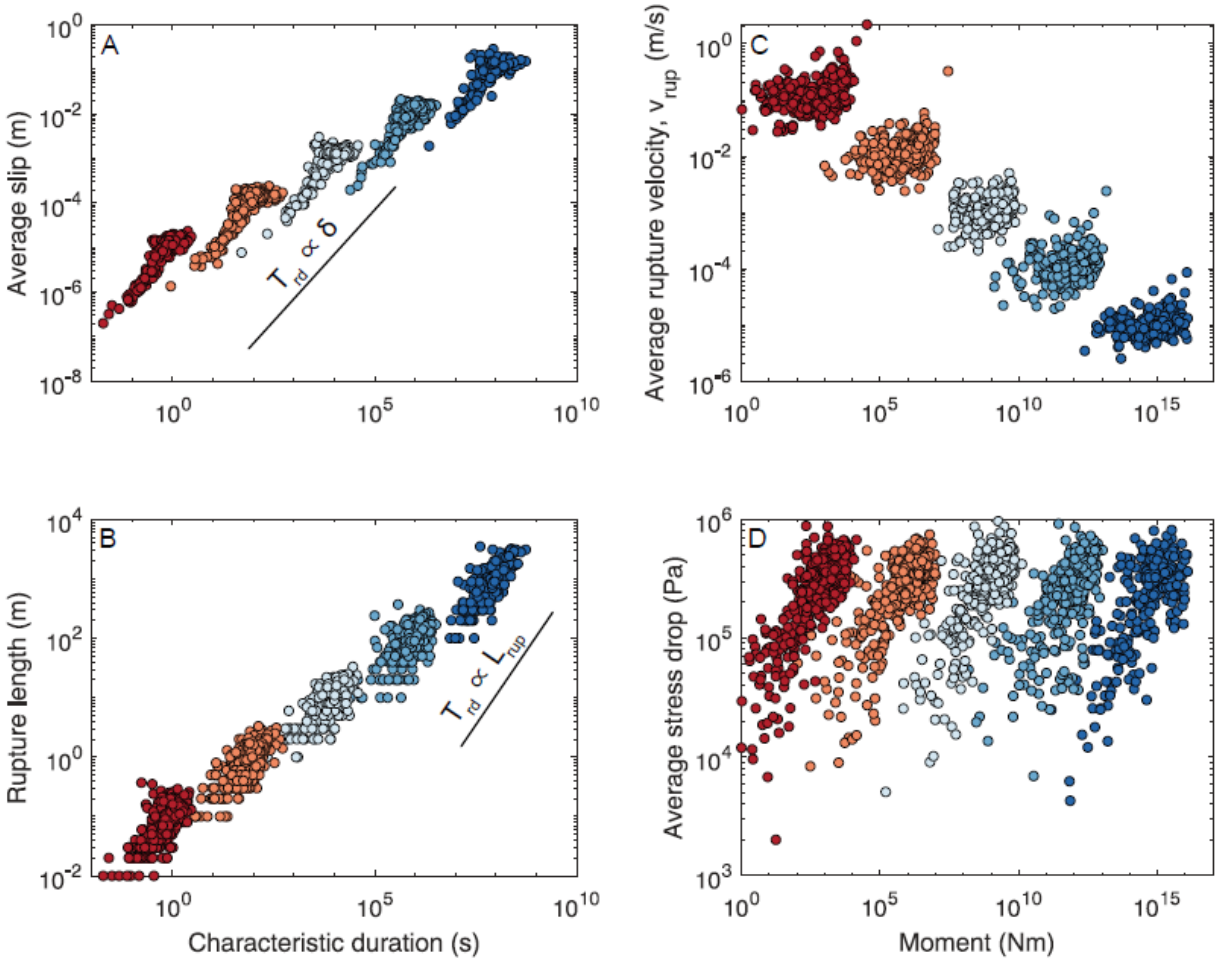

Figure S6. Source properties of ruptures in the numerical model. Each set of models is defined by a fault zone width (H) and friction distance Dc as shown in Figs. S1-S3. Note that **(A)** Rupture-averaged slip and **(B)** rupture length increase roughly linearly with slip event duration for a given model and for a range of models. Panels **(C)**shows that rupture velocity has no apparent dependence on moment for a given numerical model whereas progressively larger moment events produce lower average rupture velocity. Finally, note that for a given numerical model **(D)**, the fault-averaged stress drop increases with moment, while for a range of fault zone widths, stress drop is independent of moment. Colors follow marker legends in Fig. 4.

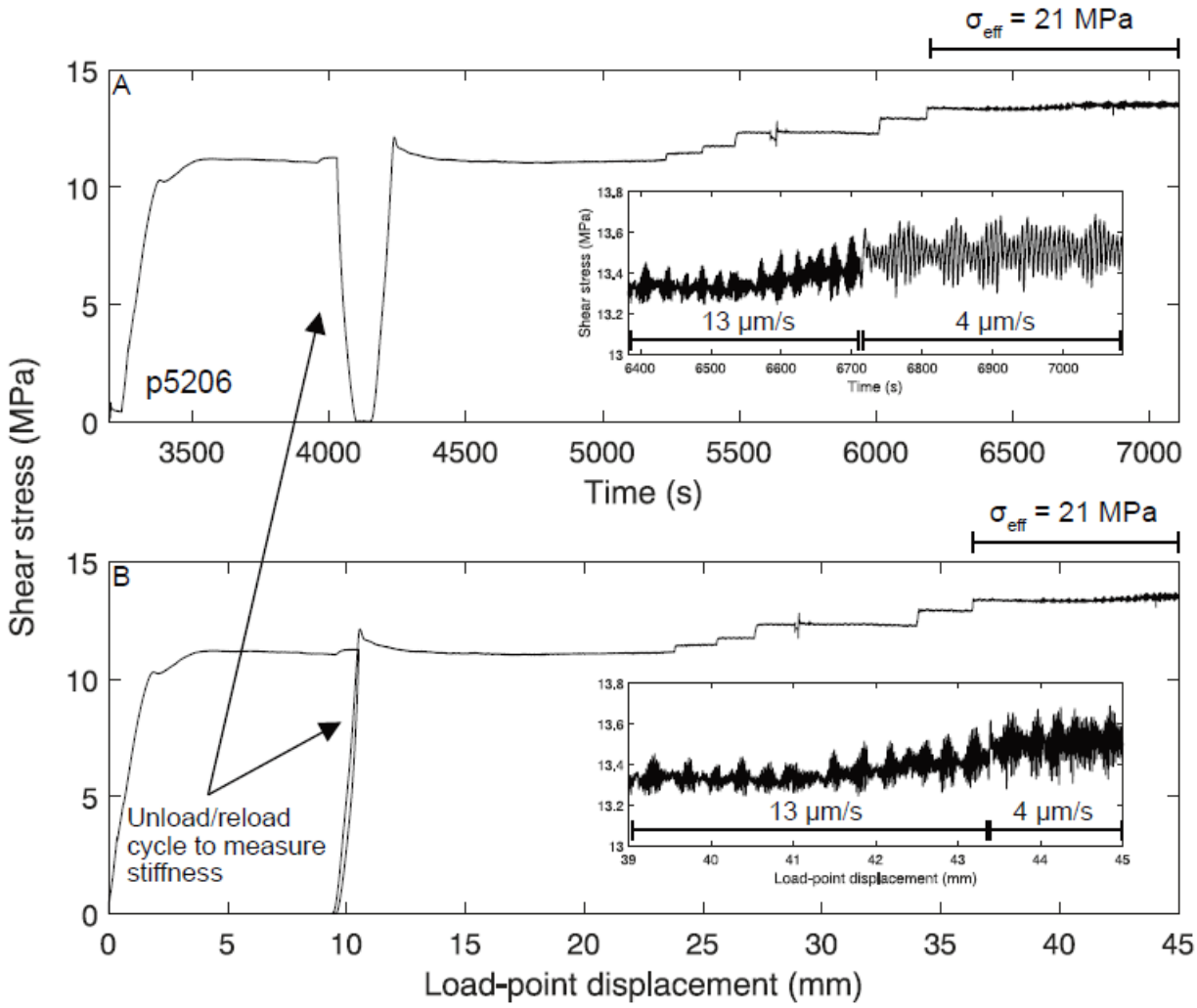

Figure S7. Data for laboratory SDS friction experiment p5206. Note that the evolution of shear stress with **(A)** time and **(B)** load-point displacement shows the initial elastic loading and the onset of slow frictional instabilities at two different loading velocities. Inset to panels **(A)** and **(B)** show sections of slow frictional instabilities at the two loading velocities.

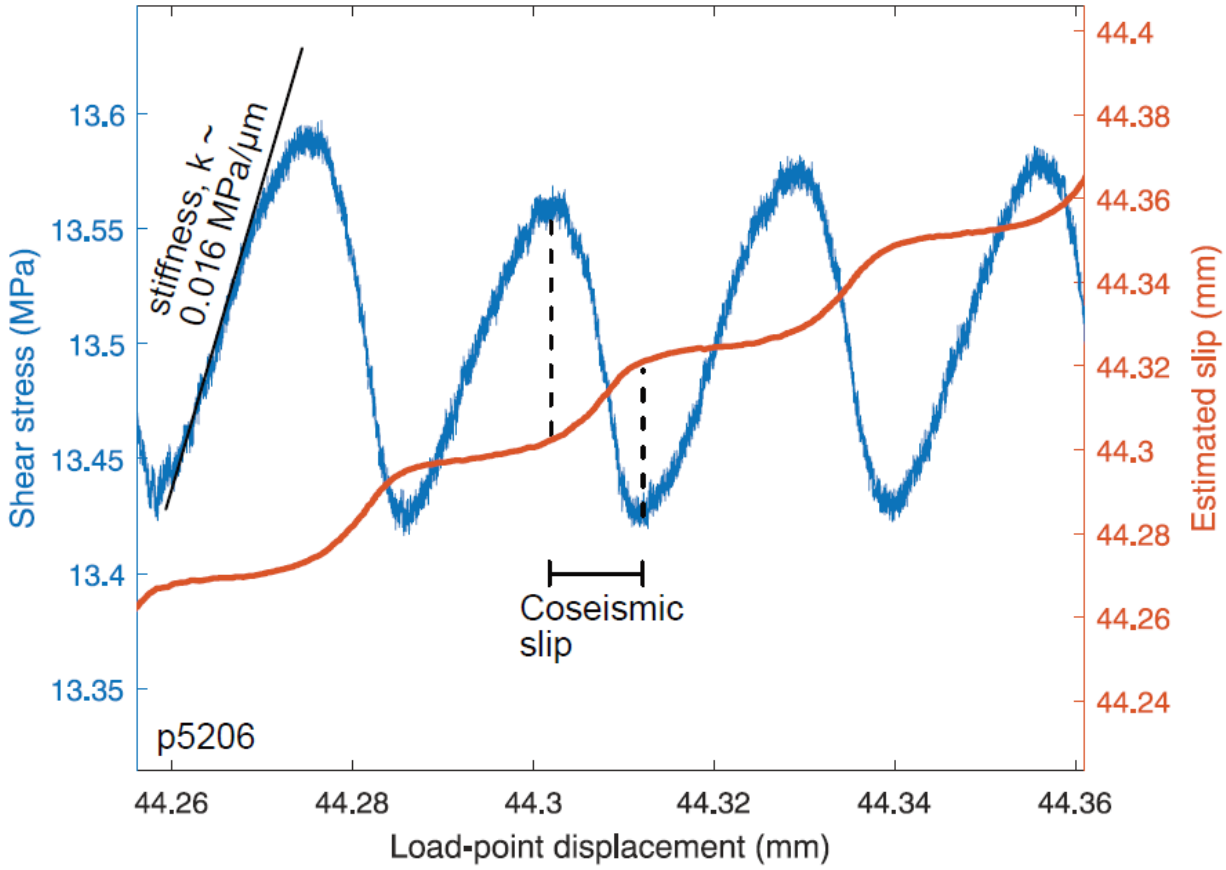

Figure S8. Estimation of slip and loading stiffness for an SDS experiment. The loading stiffness (red) is estimated as the linear portion of shear stress increase over load-point displacement, and the co-seismic slip is calculated as the amount of slip between peak stress and minimum stress during a stick-slip. This stiffness value is used to derive the loading modulus for the numerical value.

Table S1. Elastic and frictional properties used to simulate the laboratory friction experiment

Name	Value	Source
Elastic parameters		
Shear modulus of gouge, G	200 MPa	Friction experiment p5206
Acrylic spring elastic modulus, G_p	5.33 GPa	Friction experiment p5206
Bulk modulus of gouge, K	1 GPa	(1)
Density of gouge, ρ	1600 kg/m^3	(1)
Fault thickness, H	3 mm	Friction experiment p5206
Acrylic spring length, L_p	80 mm	Friction experiment p5206
Frictional parameters		
Base friction, μ_0	0.64	(2)
Frictional stability, a-b	-0.0031	(2)
RSF parameter, b	0.012	(2)
Characteristic slip distance, Dc	1.8 μm	(2)
Boundary conditions		
Effective normal stress, σ_{eff}	21 MPa	Friction experiment p5206
Loading rate, v_{plate}	4 μm/s, 13 μm/s	Friction experiment p5206
Fault length, L	5 cm	Friction experiment p5206
Mesh size, Δx_i	L/50	-

Table S2. Elastic and frictional properties used in the suite of fault zone models

Name	Value
Elastic parameters	
Shear modulus, G	10 GPa
Bulk modulus, K	22 GPa
Density, ρ	2650 kg/m^3
Fault thickness, H	15 cm, 1.5 m, 15 m, 150 m, 1.5 km
Frictional parameters	
Base friction, μ_0	0.64
Frictional stability, a-b	-0.004
RSF parameter, b	0.012
Characteristic slip distance, Dc	2 μm, 20 μm, 200 μm, 2 mm, 20 mm
Boundary conditions	
Effective normal stress, σ_{eff}	21 MPa
Fault length, L	50 cm, 5 m, 50 m, 500 m, 5 km
Mesh size, Δx_i	L/50

SI References

1. Kenigsberg, A. R., Rivière, J., Marone, C., & Saffer, D. M. (2020). Evolution of elastic and mechanical properties during fault shear: The roles of clay content, fabric development, and porosity. Journal of Geophysical Research: Solid Earth, 125(3), e2019JB018612.
2. Leeman, J. R., Saffer, D. M., Scuderi, M. M., & Marone, C. (2016). Laboratory observations of slow earthquakes and the spectrum of tectonic fault slip modes. Nature communications, 7(1), 1-6.